Received November 29, 2021, accepted December 30, 2021, date of publication January 6, 2022, date of current version January 13, 2022.

Digital Object Identifier 10.1109/ACCESS.2022.3140645

Prognostics for Electromagnetic Relays Using Deep Learning

LUCAS KIRSCHBAUM[1], VALENTIN ROBU[2,3], JONATHAN SWINGLER[1], AND DAVID FLYNN[1,4], (Member, IEEE)

[1]Smart-Systems Group, School of Engineering and Physical Science, Heriot-Watt University, Edinburgh EH14 4AS, U.K.
[2]CWI, Dutch National Research Institute for Mathematics and Computer Science, Intelligent and Autonomous Systems, 1098 XG Amsterdam, The Netherlands
[3]Algorithmics Group, Electrical Engineering, Mathematics and Computer Science, Delft University of Technology (TU Delft), 2628 XE Delft, The Netherlands
[4]James Watt School of Engineering, University of Glasgow, Glasgow G12 8QQ, U.K.

Corresponding author: Lucas Kirschbaum (lpk1@hw.ac.uk)

This work was supported in part by the Engineering and Physical Sciences Research Council (EPSRC) Centre for Doctoral Training in Embedded Intelligence, U.K., under Grant EP/L014998/1; in part by Baker Hughes; and in part by the Lloyds Register Foundation under Grant AtRI100015.

ABSTRACT Electromagnetic Relays (Electromagnetic Relay (EMR)s) are omnipresent in electrical systems, ranging from mass-produced consumer products to highly specialised, safety-critical industrial systems. Our detailed literature review focused on EMR reliability highlighting the methods used to estimate the State of Health or the Remaining Useful Life emphasises the limited analysis and understanding of expressive EMR degradation indicators, as well as accessibility and use of EMR life cycle data sets. Prioritising these open challenges, a deep learning pipeline is presented in a prognostic context termed Electromagnetic Relay Useful Actuation Pipeline (EMRUA). Leveraging the attributes of causal convolution, a Temporal Convolutional Network (TCN) based architecture integrates an arbitrary long sequence of multiple features to produce a remaining useful switching actuations forecast. These features are extracted from raw, high volume life cycle data sets, namely EMR switching data (Contact-Voltage, Contact-Current). Monte-Carlo Dropout is utilised to estimate uncertainty during inference. The TCN hyperparameter space, as well as various methods to select and analyse long sequences of multivariate time series data are investigated. Subsequently, our results demonstrate improvements using the developed statistical feature-set over traditional, time-based features, commonly found in literature. EMRUA achieves an average forecasting mean absolute percentage error of ± 12 % over the course of the entire EMR life.

INDEX TERMS Electromagnetic relay, prognostics, prognostics and health management, predictive maintenance, remaining useful life, artificial intelligence, deep learning, temporal convolutional networks, Monte-Carlo dropout.

ABBREVIATIONS

AT	Arcing time.
BT	Bounce time.
CAE	Convolutional auto encoder.
CC	Coil current.
CI	Contact current.
CNN	Convolutional neural network.
CR	Contact resistance.
CT	Closing time.
CV	Contact voltage.
DCR	Dynamic contact resistance.
DI	Degradation indicator.
EI	Exponential indexing.
EMR	Electromagnetic relay.
EMRUA	Electromagnetic relay useful actuation pipeline.
EOL	End of life.
FC	Fully connected layer.
GI	Growing-sequence indexing.
LI	Linear indexing.
LSTM	Long-short-term-memory network.
MAE	Mean absolute error.
MAPE	Mean absolute percentage error.
MCD	Monte-carlo dropout.
MVTD	Multivariate time series data.
NN	Neural network.
OT	Over-travel time.

The associate editor coordinating the review of this manuscript and approving it for publication was Sajid Ali.

PdM	Predictive maintenance.
PT	Pick-up time.
ReLU	Rectified linear unit.
RMSE	Root mean squared error.
RNN	Recurrent neural network.
RT	Release time.
RUA	Remaining useful actuations.
RUL	Remaining useful life.
SOH	State of health.
ST	Super-path time.
TCN	Temporal convolutional network.

I. INTRODUCTION

The EMR is a versatile component found in many electrical systems e.g., consumer products or safety critical applications in the nuclear- or aviation industry. Over several decades, EMR failure modes and mechanisms in particular relating to electrical contact degradation have been subject of extensive studies [1], in order to improve design and material properties [2]–[4].

Automation has supported an improvement in EMR manufacturing and reliability. Population based methods have proven to be a cost efficient solution to determine the reliability of bulk produced EMRs [5], [6]. In fact, based on our analysis of the academic literature and industrial trends - to the best of our knowledge - the predominant effort to date aims to quantify the degradation of EMRs using classical reliability theory. However, in many safety and mission critical applications an EMR will be subjected to direct and indirect ambient loading that is specific to the application, rather than being in conformance to generalised operational requirements expected of bulk produced quantities. Therefore, these EMRs are precision engineered for their very specific application, cf. [7], [8]. Such applications might not align with the classical reliability methods that rely on large sample sizes and run-to-failure data [9]. Furthermore, the use of predefined life cycle estimates for maintenance management schemes often results in early replacement of operationally viable EMRs [10]. Classical reliability based testing methods have been increasingly challenged in terms of test duration by the extended durability of the current generation of EMRs [6]. Lastly, the objective of past research centres around the definition of expressive/ representative sDegradation Indicator (DI)s and the evaluation of those using data e.g., only from early switching actuation [11], [12]. Hence, our analysis of the state-of-the-art of EMR reliability and Prognostics and Health Management (PHM) related models reveals several distinct shortcomings, namely: computational inefficient for in-situ deployment; limited transferability as a result of poor performance generalisation; models have been predominately trained on constrained data sets and feature selections e.g., not representative life cycle data. Our research methodology addresses these constraints e.g., monitoring strategies that can support cost effective and application specific data acquisition and processing for accurate EMR life cycle estimation.

With respect to monitoring EMRs as part of a condition monitoring programme which sits within operational and maintenance expenditure, this has been traditionally cost prohibitive in many applications. However, in line with the digital industrialisation there is an unprecedented access to large volumes of system and component monitoring data e.g., Big Data (BD). BD and subsequent analytics have the potential to improve the derivation of enhanced EMR models for maintenance strategies [13]. Transitioning to industrial applications entails barriers though [14], [15]. Among others, uncertainty and a sensible, efficient embedding of physical, data-driven or hybrid models into existing digital infrastructure has to be considered [16]. In this scope, enabling modern maintenance strategies (cf. PHM as extensively reviewed in e.g., [17]–[19]) by creating actionable insights from data through data-driven Condition Based Maintenance (CBM) or Predictive Maintenance (PdM), is confronted with high volumes of Multivariate Time Series Data (MVTD). With the advent of Artificial Intelligence (AI), research is addressing this challenge using Machine Learning (ML) and increasingly Deep Learning (DL) for e.g., Remaining Useful Life (RUL) prediction of electronics [20]–[24]. Standalone approaches relying on Convolutional Neural Network (CNN) architectures or in combination with Recurrent Neural Network (RNN) elements employing techniques such as multivariate-time-series imaging [25] resonate with high volumes of MVTD as recent publication demonstrate [26]–[32]. In particular, approaches utilising CNN, typically as Convolutional Auto Encoder (CAE) for automated feature extraction whilst drawing on the auto-regressive power from RNN-based architectures e.g., Long-Short-Term-Memory Network (LSTM), are popular combinations [33], [34]. Though, a substantial amount of research exploits DL for RUL estimation, these methods are limited in terms of scalability when it comes to high data volumes; in addition very long input sequences pose a challenge. TCN, initially presented by [35] addresses above shortcomings. TCN performs dilated, causal convolution - transforming CNN to highly efficient, auto-regressive models as evidenced by [35]–[37]. Unlike e.g., LSTM, TCN is able to be trained on input sequences, irrespective of the length as the number of trainable parameters per layer only depends on the number of input features, filters and the kernel-size.

Due to above advantages, TCN is subject to an increasing interest in PHM as the body of recent literature demonstrates. TCN has been used for RUL estimation as an alternative to RNN by [38]–[40] on the turbofan-engine degradation *NASA C-MAPPS* data-set [41]. Degradation estimation of bearings using TCN is evaluated and benchmarked on the *PRONOSTIA* bearing data-set [42] presented by [43], [44]. A method based on TCN for State of Health (SOH) and remaining number of charging cycles estimation of lithium-ion batteries is presented by [45], evaluated on the *NASA lithium-ion battery* data-set [46]. Lastly, [47] proposes a

combination of CAE and TCN for robust feature extraction and RUL estimation in the context of critical nuclear power plant infrastructure, namely electric valves.

However, despite the reported improved performance of TCN compared to e.g., CNN-LSTM, so far none of the reviewed approaches considers uncertainty quantification. Though, without addressing uncertainty the applicability of any PHM method is questionable [17], [18]. Methods for uncertainty estimation integrated in DL architectures have been presented by e.g., [48]. A Bayesian approximation to estimate predictive uncertainty has been proposed by [49], referred to as Monte-Carlo Dropout (MCD), evaluated in the context of PHM by [50], [51].

Extending our earlier work in [52], this research develops a novel data-centric, streamlined DL prognostics approach for EMR that reduces the need for tedious Contact Resistance (CR) measurements, relying solely on Contact Voltage (CV) and Contact Current (CI) waveform records of switch-on and switch-off events - monitoring data readily available in many industrial systems. This research's central objective is the estimation of the EMR-Remaining Useful Switching Actuations (RUA) (i.e., the number of remaining useful switching actuations till the EMR fails) under consideration of predictive uncertainty. Therefore the EMRUA pipeline is proposed. The hierarchical TCN-based prognostics approach aids the development of novel data-driven maintenance schemes such as PdM allowing component-tailored maintenance under consideration of past and present operating conditions. To facilitate the development of the EMRUA, a set of EMR life cycle experiments have been conducted. Subsequently a range of input features is derived and its performance is extensively evaluated.

This paper is structured as follows: Section II provides an in-depth discussion of EMR failure modes, failure mechanisms and the types of traditional DIs used to quantify the state of EMR degradation. Section III reviews the state of the art on research concerned with EMR reliability, SOH and RUL for various applications settings. Subsequently, we elaborate on the developed prognostics methodology in Section IV. Experimental considerations and the results are discussed in Section V. Lastly, Section VI summarises the findings.

II. BACKGROUND

The main task of an EMR is the electrical separation of the control- from the load-circuit [53]. An EMR typically consists out of a magnetic coil, a travel armature, a spring and a contact pair. Though, the EMR has been subject to considerable design improvements over the past decades, the core components and working principle remain essentially unchanged, cf. Fig. 1.

Despite the availability of electrical switching devices e.g., Metal Oxide Semiconductor Field Effect Transistor (MOSFET)s or Solid-State-Relays without mechanical parts exhibiting an improved reliability [7], the EMR puts a set of distinct characteristics forward. It features an overall low

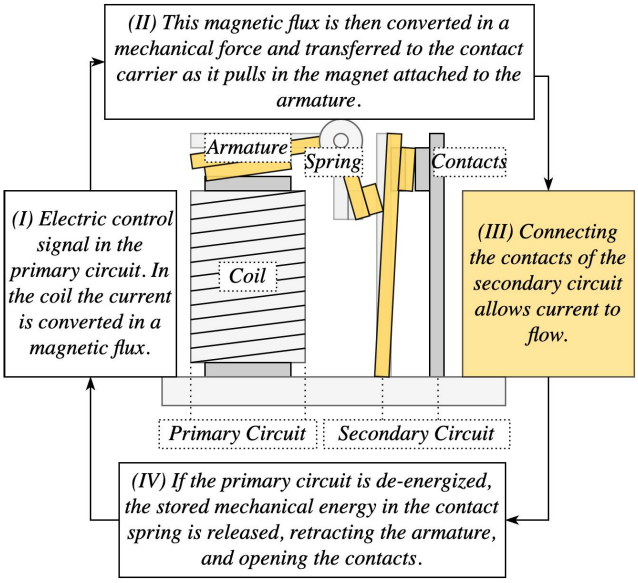

FIGURE 1. Schematic display of the function and main components of a traditional EMR, adopted from [53].

CR - typically in the $m\Omega$ range reducing switching losses; high breakdown voltage of up to 1000 V; total isolation of the switching and control circuit [53], [54]. Latter one is not the case for most semiconductor based switching components. EMRs can be employed where switching is independent from the current direction. For example, EMR are commonly the preferred choice in safety critical applications within nuclear power plants as they can be run in a *fail-open* fashion [8]. However, despite miniaturisation efforts, EMRs are large compared to other electrical components and switching speed is slow - in the ms range compared to MOSFET in the ns or Solid-State-Relays < 0.2 ms range [1].

A. FAILURE MODES

Due to the electro-mechanical nature of the EMR, its life is dependent on the mechanical as well as the electrical life of the individual subcomponents. The mechanical life is typically in the order of 10^7 actuations compared to the electrical life at 10^6 actuations [1]. An EMR is considered failed i.e., its End of Life (EOL) if it can no longer perform its specified switching function. Electrical, contact related failures prevail, such as elevated CR. Making or breaking-contact related failures are the predominant failure modes in EMR applications [10], [55]–[57]. Though one can distinguish failure modes by type, multiple of the failure mechanisms interact, as the following Section demonstrates.

1) CONTACTS

Contact related failures typically occur over a long duration. Such failures depend on the applied voltage and current, load type, the temperature as well as the pollution of the operating environment. The root-causes for contact failures are excessive material-transfer and -loss due to electrical arc discharge

TABLE 1. Contact related failure modes and mechanisms.

Modes & Mechanisms	Causes
Making Failure	
Reduced Contact Force	Excessive contact material loss due to e.g., electrical erosion.
Mechanical Fatigue	Reduction in spring force; bent or stuck armature.
Breaking Failure	
Welding and Bridging	Arc discharge during bouncing and a reduction in contact force.
Mechanical Fatigue	Stuck armature.
High Contact Resistance	
Contact Erosion	Contact surface roughness increases due to ongoing material loss and material redeposition from electrical arcing reducing the effective contact area.
Fretting	Deposition of material on the contact surface (partially insulating) due to mechanical wear.
Contamination	Corrosion; film-formation from various sources e.g., organic particles, oxides, carbides.
Extended Operate and Release Time	
Micro-Welding	Formation of small, weak welds during contact bouncing cause the contacts to stick together.
Coil Fatigue	Increase in CR due to e.g., wear of insulation material from long exposure to elevated temperature, subsequently increases the required pick-up voltage.
Spring Fatigue	Reduction in spring forces causes a reduced pull-in force and therefore a reduction in contact velocity.

and contact bouncing [10]. A symptom of contact erosion is reduced contact force and increased CR. Further, welding, bridging or sticking of contacts as well as corrosion and contamination - through deposition of isolating and semiconducting films, stemming from eroded or worn contact material, carbides dissolved from organic gases - are the governing failure mechanisms. Such mechanisms lead to making and breaking failures, impermissible operate and release times respectively, an increase of CR beyond an acceptable range, and high levels of contact noise [53]. An overview of the contact related failure modes is provided in Table 1.

a: MAKING FAILURE

The inability to make a connection whilst the CR remains below the maximum specified CR. If the application setting is favourable for electrical arcing, the likelihood of a making failure due to erosion and the subsequent material transfer is high [56]. In some instances an increasing CR can point to an impending making failure. However, the actual failure starts to develop when erosion has well-advanced and the Over-Travel Time (OT) respectively the contact force have become to small to enforce good contact making, often exhibiting an increase in Bounce Time (BT) [1]. However, making failure can also be caused by preceding mechanical failures, such as a spring failure, a bent armature or coil failure.

b: BREAKING FAILURE

The inability to break a connection and interrupt the current flow within the specified maximum opening time. If contacts are switched under load, contact bridging due to contact welding can occur. If contacts are welded together, CR is lower than specified minimum CR for open contacts. Mechanical failures preventing the contact from opening can relate to spring or armature failures.

c: OPERATE- & RELEASE-TIME FAILURE

The duration to make or break contact exceeds a maximum specified threshold. If the Release Time (RT) increases, this can be due to the spring degradation, reducing the contact pull force. However, more likely are local micro-welds across the contacts surface, causing the EMR contacts to stick. Pick-Up Time (PT) and RT both can increase if the coil operating voltage changes due to coil deterioration [58].

d: ELEVATED CONTACT RESISTANCE

Unacceptable high CR while contacts are closed. Manufacturers specify the maximum acceptable CR for closed contacts. Such CR is typically in the $m\Omega$ range. In general different interacting factors influence the CR, which can be distinguished by either having a decreasing or increasing effect. During operation, under low-load, changes of CR are dominated by mechanical effects, despite occasional increases of CR through e.g., polymerisation or corrosion on the contact surface. However, if the amount of carried current increases - and the contact temperature respectively - continuous electrical fatigue due to arc erosion reduces the contact force inevitably. In such instances, film formation in combination with corrosion becomes the dominating degradation regime. A subsequent reduction of the effective contact area leads to a significant increase of CR. Unsealed EMRs, operated in high temperature environments are also liable to serious rates of contact oxidation. Mechanical actuation i.e., contact making and breaking, can rupture deposited films reducing CR [59]. Effects like ion-sputtering might temporally clean the contact surface and reduce CR. An increase in CR is often accompanied by contact noise.

2) COIL AND MECHANICAL PARTS

a: COIL

Long-term use impacts the coil resistance. Deposition of evaporated contact material particles on the coil wire or combustion of the insulation material due to excessive heat reduce the coil's insulation resistance [60]. Further, poorly welded coil wires might be a failure root-cause. In general, coil failure is most likely to happen if the ambient temperature is high causing the coil to overheat. Typical failure modes are a shorted coil or changes in the pick-up or release voltage. However, it should be noted, that the likelihood of these failures is very low in comparison to the failure modes directly relating to the contacts.

b: MECHANICAL PARTS

The wear of mechanical parts e.g., the armature or spring, causes a reduction in contact force or variations in contact

velocity. This wear stems from material fatigue due to vibrations or excessive heat e.g., from high-current arc discharges.

B. FAILURE MECHANISMS

This section elaborates failure mechanisms relevant to the EMR contacts. Essentially, all failure mechanisms contribute to a change in CR, ultimately leading to one of the listed failure modes.

Though, not obvious to the eye, the nominal contact area is not the true conductive contact area. The inherent microscopic surface roughness restricts the path of the current flow [1], [61]. The *actual* contact points are referred to as *a-spots*. The observed increase of CR through this limited interface compared to the resistance via the apparent contact surface is referred to as constriction resistance and subject to the elastic and plastic properties of the contact material. The interested reader can refer to [53], [62] for extensive discussion of the contact related resistance and appropriate methods to approximate CR in different contact settings. In general, low contact forces result in high CR. In industrial applications CR is deemed unacceptable if the contact force is below $> 0.05N$ [53].

During contact switching the CR will increase if the power increases, up until the softening voltage is reached. A temperature differential can be observed between the *a-spots* and the contact body. The contact material is subject to plastic deformation at the conducting *a-spots* as Joule-Heating causes a local temperature increase. Plastic deformation increases the effective contact area, causing a drop in CR. If the voltage continues to rise, the CR increases again, till the melting point of the contact material has been reached. A rapid increase in the effective contact area can be observed going hand in hand with a secondary decrease in CR [53]. This effect is sometimes referred to as *self-healing* of contacts [1]. Predominant failure mechanisms are discussed in the remainder of this Section.

1) DC ARC EROSION

Primarily, due to the heating of the contact material to its boiling point, electrical arcing consequentially leads to an electrical erosion across the contact surface, predominantly affected by the operating mode and the type of electrical load [1], [2], [63]–[65]. The material redistribution process electrical contacts in Direct-Current (DC) circuits are subjected to is a continuous net transfer from one contact to the other resulting in a so-called pip and crater structure on the surface. Whether the pip and crater are located on the cathode or anode depends on the duration and energy of the arc, the circuit inductance, the contact material, the switching speed of the contacts, the cleanliness of the contact surface, and the contact dimensions [1]. The rate of material erosion will increase as the energy and duration of the arc increases.

Erosion during the stage of the metallic-arc and during the gaseous-arc can be distinguished, cf. Fig. 2. During the metallic-*pseudo*-arc, after the rupture of the molten metal bridge (cf. Appendix D), the gross of current is transferred by

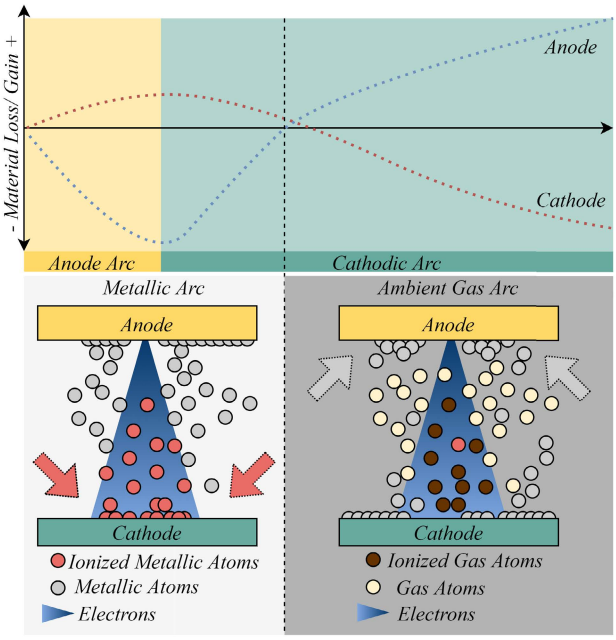

FIGURE 2. Schematic display of the erosion processes at cathode and anode during the phase of electrical arcing in metallic vapour and in ambient air.

metal ions. Hence as [66], [67] demonstrate, a material gain at the cathode stemming from the vaporised and subsequently ionised metal atoms can be observed. Simultaneously at the anode electron bombardment leads to electron sputtering disintegrating anode material. Hereinafter, the electrical arc will transfer to an arc in ambient air as the density of the metallic vapour decreases. The arc is now predominantly ionising the ambient gas atoms. The impact of the ionised gas atoms will erode material on the cathode, called gaseous ions sputtering [68]. An increasing net gain at the anode can be observed as the metallic atoms - separated from the cathode contact surface through the impacting gaseous ions - aggregate at the anode region. In general, in DC circuits a cathode gain - material build up (pip) - can be observed with short arcing times, as the duration of the arc operating in ambient air is relatively short in comparison to the metallic-arc. With increasing arcing duration, an anode pip and a cathode crater will become more likely.

Bouncing during contact making is a common phenomenon, due to the preserved kinetic energy of the closing contacts, cf. Appendix C-A. Besides its relevance to contact welding as elaborated in Section II-B2, erosion effects stemming from high frequent bouncing - many short bounces - accelerate erosion through arcing and the formation of pip and crater structures [69]. However, if bouncing is neglectable, the bulk of contact erosion will take place during contact breaking. Shortening the arc duration through higher opening speeds therefore reduces arc erosion [70]. Though, this might lead to more bouncing and therefore erosion during contact making respectively.

To conclude, the combined material loss and re-deposition effects during electrical arcing of opening or closing contacts

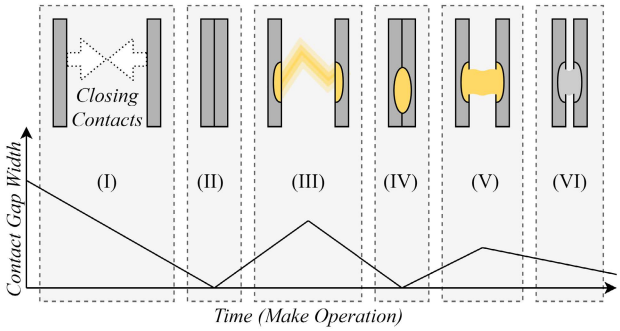

FIGURE 3. Schematic display of the welding process of closing contacts subjected to arcing. (I) Contacts close; (II) due to the preserved kinetic energy contacts bounce the first time; (III) the voltage drops to the minimum arc voltage and an arc forms, heating up the contact material on the anode and cathode fall region; (IV) the contacts close on the molten metal pools; (V) as the contacts open for the second bounce, a weld forms; (VI) if a weld establishes and cools down quickly, its strength might be greater then the remaining kinetic contact force. It prevents the contacts from closing or opening again.

in DC applications is the sum of material lost through ejected metal droplets at the arc roots, a continuous material redistribution process, and dispersed metal vapour after the rupture of the molten metal bridge [2]. Contact erosion leads to a deterioration of the contact surface and thereby to a reduced effective contact area when contacts are closed. The problem is aggravated as the contact force is reduced due to the contacts material loss, likewise contributing to contact welding as discussed in the following Section.

2) CONTACT WELDING

When the contacts part, local Joule-Heating heats up the contact material, leading to a locally constrained melt and a sequential weld, illustrated in Fig. 3. Welding is critical if the contacts can no longer part i.e., stuck-closed failure [71]. Though, welding during contact breaking is possible, it is not very likely [72], [73]. On the contrary, the problem of contact welding during contact making is exacerbated if contact bouncing and *pre-strike* arcing are present, cf. Appendix C-A. As the contacts open and close upon molten metal interfaces a weld is formed. This weld is problematic if the contact force is reduced prior to the contacts being fully closed. A reduction in contact velocity provides more time for the weld to cool down and harden [74].

Relevant to the welding strength is the load current and the duration of the bounce. The strength of the weld increases with the amplitude of the applied current [4]. As bouncing events become shorter with each subsequent bounce an increase in the weld strength for late bounce events, somewhat growing exponentially past the 4^{th} bounce can be observed [75]. Further effects of welding during bouncing are discussed in [1], [71].

3) CONTACT CONTAMINATION

In addition to the effects of contact shape and constriction resistance, the CR is effected by the film resistance, a problematic thin film layer build up on the contacts. Such isolating or semiconducting layers can be deposited on the contact surfaces through e.g., outgassing of plastic sealings or insulation materials, material abrasion, and contamination from the ambient air. Thus, the actual number of conducting *a-spots* is further reduced, leading to a CR build up [61]. Subsequently, electrical conduction can only take place at spots where this film is ruptured during contact making. Isolating barriers are destroyed either electronically or mechanically through increased contact forces. As [53] reports, already very thin films (>10 nm) can cause high CR. However, semiconducting films can also contribute to an increase of the effective contact area in some instances. The extent of film formation depends on the storage duration, the environment, the operational conditions and the alterations to the contact surfaces from electrical arcing.

A major source for surface film contamination is silicon. Its compounds are commonly found in e.g., lubrication, insulation material, paints or plastic components, such as EMR enclosures. Vapours emitted from those silicon containing materials can form insulating films, which deposit on the contact surface [76], [77]. During switching, due to electrical arcing, silicon breaks down to silica (silicon-dioxide), compromising contact performance, significantly increasing CR towards the EMR-EOL [78]. Further effects of particles stemming from contaminated environments and the effects of *fritting* - a sudden breakdown of the CR in the presence of contaminating films are discussed in [1], [79] as well as Appendix B.

4) FRETTING

Lastly, contact surfaces are liable to *fretting* [80], [81]. Fretting contributes to the wear of the contacts as the mutual displacement of the contacts against each other contributes to the abrasion of the surface producing debris. Fretting can be due to external vibrations or different rates of thermal expansion of the contact materials. It increases CR and promotes other degradation mechanisms, contributing to CR fluctuations over the EMR life as well as an increase in contact noise [53]. The process is detailed in Fig. 4.

C. CONTACT RESISTANCE DI

Various measures to determine and depict degradation, in particular the electrical life subjected to contact degradation, in EMR applications have been developed [7], [56]. The following sections reviews the advantages and disadvantages of classical DIs.

1) CONTACT RESISTANCE DI

The most popular measure among the developed DIs is CR [83]. However, as the initial CR is already very small, the increase till failure is typically within the $m\Omega$-range. This poses a challenge for accurately measuring changes in CR, which can be achieved reliably only with a *4-Wire* or *Kelvin-Wire* setup [78]. Therefore, presupposing accurate CR measurements in embedded online health management is

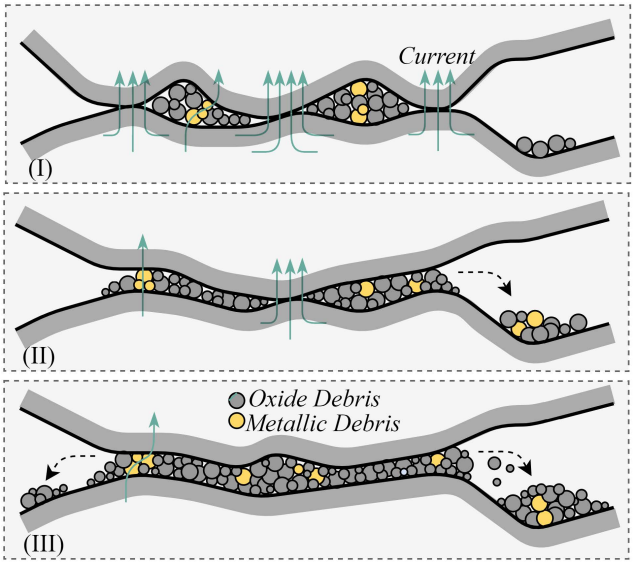

FIGURE 4. Schematic display of the process of closed contacts subjected to fretting. (I) Accumulation of partially and fully oxidised metallic particles on the rough contact interface restricts the current flow to the current carrying *a-spots*, affected by the distribution of surface asperities [82]. Some temporary current carrying paths may establish through metallic and partially oxidised particles in the debris matrix [1]. (II) Over the course of operation the contact surface further degrades, reducing the effective contact interface, accumulating debris and increasing CR. (III) A significant increase in CR is observable. No direct contact is made due to the amount of accumulated debris. Current conduction takes place along isolated paths in the debris matrix made up of non-oxidised particles, subjected to immediate changes as material is further displaced.

not a viable solution due to the required sensing hardware and associated costs. In addition, depending on the type of EMR, CR is subjected to more or less random fluctuations ranging well above the rated maximum acceptable CR, masking underlying trends and rendering the definition of a static CR-based EOL threshold unfeasible. The rate and intensity of these fluctuations depends on the operating pattern and the load, but foremost on the contact material and environment [84]. Hence, the overall degradation is often not reflected in CR [7], [85]. The Appendix E discusses the aspects of CR fluctuations in detail.

2) ALTERNATIVE DIs

Above mentioned challenges as well as the need to distinguish failure modes from recorded data motivated the search for alternative DIs. Developed DIs depict EMR wear and can be distinguished in two groups namely (1) *non-intrusive* time-based reference DIs and amplitude-based reference DIs, as well as (2) *intrusive* DIs which require dissembling the EMR or extended sensing capabilities.

a: NON-INTRUSIVE DIs

Such DIs predominately rely on the measurement of CV and Coil Current (CC) waveforms during contact making and breaking. Processing these signals allows to derive a set of measures displayed in Fig. 5. As for time-based-reference

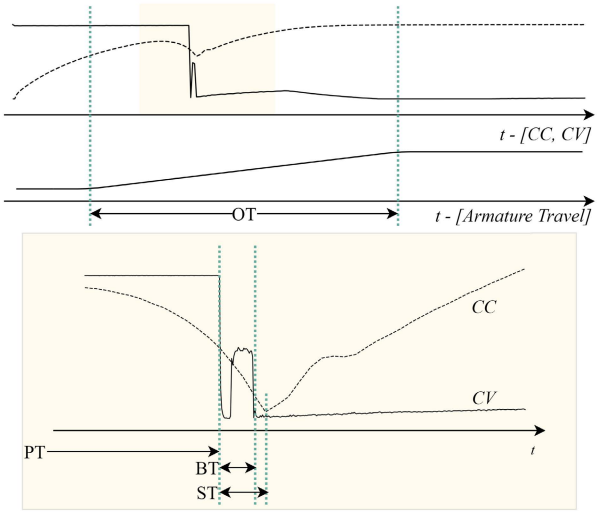

FIGURE 5. Selected time-based reference DIs derived for contact making of a normally open EMR. Pick-Up Time [PT], Bounce Time [BT], Super-Path Time [ST], Over-Travel Time [OT].

DIs, naming convention throughout literature is somewhat ambiguous and depends on the type of contact configuration [86].

The trajectory of time-based reference DIs varies in respect to the experienced failure mechanism and failure mode, the design of the EMR and the operational environment [6], [58], [60]. Thus, as Section III demonstrates, no generally valid non-intrusive DI has been established throughout the body of research. Nevertheless, DIs can provide application-specific, valuable information regarding the progress of EMR degradation. An overview of EMR time-based reference DIs and amplitude-based reference DIs is provided in Table 2.

b: INTRUSIVE DIs

Various research has utilised intrusive measurements to describe and quantify EMR contact degradation e.g., the mass transfer by detaching and weighing the contacts at regular intervals [91]. Alternatively, radioactive tracers can support understanding material transfer among switching, arcing contacts [1]. Further analysis of contact surface at different stages using Energy Dispersive X-Ray (EDX) and Scanning Electron Microscopy (SEM) have been used [54], [92]. In [93] the arc discharge is optically monitored. Lastly, measurements of static and dynamic contact pressure enable an assessment of the contact health [94]. While such DIs are able to depict the degradation, obtaining these measurements at scale outside controlled laboratory environments is often impractical [86], [91].

III. RELATED WORK

A. GENERAL DC EMR

In [95] various contributing EMR failure mechanisms are analysed, on which basis the authors extend their research towards a predictive maintenance approach in [85], focusing on prediction of the CR degradation trajectory.

TABLE 2. An overview of classical EMR-DIs.

Time-based reference DI	
Pick-Up Time (PT)	The time between the increase of coil voltage and the first CV drop during making. BT is not considered [12]. For example, [87] report if coil wire resistance increases, the magnetic force decreases causing a slower movement of the armature and therefore an increase in PT. On the contrary, if the spring force decreases due to ageing stress relaxation, PT decreases.
Over-Travel Time (OT)	The time between the armature/ contact start of travel and the complete closure of the armature [60]). For example, [84] report decreasing OT till stuck-open failure as the contacts erode and the subsequent armature over-travel becomes too small to force proper contact make. Likewise [6] reports decreasing OT for eroding contacts. However, if contact sticking/ welding is predominant OT is likely to increase.
Arcing Time (AT)	If CV is between the limits of 10 % and 90 % of the open circuit voltage during contact breaking [56]. The effective start of the arcing duration depends inter-alia on the minimum arcing-voltage of the contact material.
Bounce Time (BT)	The interval between the CV drop during contact making and the last bounce i.e., the CV settles. The start of BT is sometimes specified at 90 % of the open circuit voltage and if the bounce pulse is longer than 10 μs [86]. The entropy of the BT appears to correlate with the EMR-EOL [88]. BT significantly depends on the amount of contact surface wear [89].
Release Time (RT)	The time interval between the coil voltage drop/ de-energisation and the initial CV increase. BT and AT are not considered [86]. RT increases towards EOL when contacts are subject to erosion. A decreasing trend is reported in [6] if contact welding is the governing failure mechanism.
Super-Path Time (ST)	The time interval between the CV drop at the contacts and the *inductive nick* of the pick-up CC at the coil during contact making [12]. [90] finds this to be a significant DI.
Amplitude-based reference DI	
DCR	The resistance across the closed contacts just after the contacts have settled. This can be measured by recording CV and CI, though the accuracy of the used sensing equipment needs to be considered. For an extensive discussion on DCR as DI refer to [89].
Pull-In Voltage	The coil voltage at which the armature movement commences. This DI has relevance for coil failures as an increase in coil resistance can be observed via an increase in the pull-in voltage [60].
Dynamic CV	The CV drop upon first contact making.
Static CV	The CV when contact bounce has settled and contact make is established.

A Moving-Average-Model, an Auto Regressive Integrated Moving Average (ARIMA)-Model, an Exponential-Smoothing-Model, and a Neural Network (NN)-Model are compared in terms of predictive performance. Latter one is found to be best suited to predict EMR-EOL. However, the authors state that predicting the EOL solely on CR is highly application dependent and will not generalise well. [10] is concerned with improving EMR maintenance schemes, pointing out that in many instances EMR are exchanged too early, often in accordance with the predetermined life estimates. Following up on [10], [85] emphasise that dynamic CR measurements are needed in addition to static CR measurements for RUL estimation. The authors demonstrate that DCR, recorded during the closing actuation, is a valuable DI. DCR shows a comparatively more pronounced trend towards EOL. A statistical regression model to estimate the EMR life forecasting CR is presented. In [5] the authors refine their prior work, stressing the importance of alternative DIs. The authors identify promising indicators from the sensed waveform, being the DCR, maximum-CR and BT. Based on the extracted features a fuzzy model is used to evaluate contact reliability. However, no further insight into the concrete nature of the measurements nor the contact failure modes is provided. The authors reconsider their approach in [88], addressing the use of BT for estimation of the EMR performance. Analysing the entropy of the BT using sequence encoding, the extracted trend relates to the EMR life cycle and its EOL, though the analysis is performed on a fairly small data set.

The research in [6] is motivated by the need for a novel method to evaluate the EMR life, as traditional reliability methods have become too time demanding not yielding failures in reasonable test-time, due to improvements in design and quality of EMRs. The experiments conducted within the study reveal that different failure mechanisms change the shape of DI degradation trajectories, demonstrated for Closing Time (CT), RT and OT. The potential of a regression model combining the effects of the identified failure mechanisms to predict the EMR degradation process for reliability purposes is explored. In [58], the authors confirm prior findings, highlighting different characteristic trajectories of DIs for various failure mechanisms such as contact erosion, contact welding and contact contamination. An expressive DI is presented, referred to as the fluctuation coefficient i.e., the correlation between the changes in CR, PT, RT, OT, BT, and AT. After preprocessing features using wavelet decomposition a linear-model is derived for DI trajectory forecasting. The best performance is achieved for either OT and BT related degradation trajectories if the EMR is subjected to contact erosion. The subsequent model does not perform as well for contact welding and contamination failures. The developed fluctuation coefficient improves the performance for these failure mechanisms, though the reported accuracy for contamination related failures remains low. A more recent work highlights two key challenges for a broad application of PHM to EMR [60]: (1) the lack of life cycle data as there are currently only very few deployed online monitoring health management solutions for EMR; (2) the uncertainty

associated with the DIs. To address former one, simulation of EMR life cycle data is proposed. Coil and armature related failure mechanisms are simulated and e.g., compared to the measured CC waveform. A diagnostic framework is proposed using the Mahalanobis distance to discriminate between EMR operation states and failure modes respectively. [96] investigates DIs of EMRs subjected to contact welding under a DC lamp-load setting. The representative *probability density distributions* of CC and CV for different states throughout the EMR life are determined.

B. AVIATION & AEROSPACE EMR

In [7], waveform decomposition facilitates DI extraction for aerospace-EMR reliability models, improving the performance over previous methods using PT, OT and RT. In [97] the authors present a time-series based EMR life prediction method identifying CR, the CV peak voltage, BT, RT and ST as valuable DIs. A regression model in combination with optimised Wavelet-Package decomposition defining a subset of significant frequencies is derived to forecast the ST trajectory, predicting ST accurately through the second half of the EMR life. In [98], the authors show that the initial mean and variation of CR time-series measurements can be used to estimate the life of the EMR. The value of the proposed approach lies in its capability to determine whether a new EMR will perform within its specification throughout the rated life under known operational conditions based on its initial state. [11] combine a physical-model of erosion related contact degradation with CR measurements obtained from aviation EMR accelerated life cycle experiments using Kalman-Filtering. However, as recognised by the authors in [55] (also compare Appendix E), the feasibility of CR as the sole measure for the advancing EMR degradation is highly depended on the application [6], [95]. A regression model using Grey-System theory is presented in combination with a CR EOL-threshold. CR fluctuations in combination with a static threshold cause the proposed model to predict the EOL too early.

C. HIGH-VOLTAGE DC EMR

The authors in [91] review the failure modes of High-Voltage-DC EMR. The predominant failure mechanisms are contact erosion and contact welding which severity can be determined through contact mass variation measurements. However, obtaining such measurements is impractical, hence the authors propose the use of the arc charge which directly relates to the contact mass loss caused by electrical erosion. A linear relationship between the cumulative arc-charge and the EMR life is derived. The methods suitability for low-voltage application is subject to future research as the authors point out. Building up on [91], the authors in [99] analyse the correlation between contact velocity and electrical life. The authors show that the cumulative arc erosion mass under different breaking velocities increases linearly. A mean EOL threshold based on the arc erosion mass is experimentally determined.

D. RAILWAY EMR

The authors in [56], [90] present diagnostic methods for railway EMR. Wavelet-Transform for denoising of extracted DIs prior to failure classification. RUL prediction is performed using ST, BT, AT, and RT. ST and BT are identified as key DIs relating to contact erosion, contact welding and contact contamination. To account for the variance in the derived DIs, the authors propose the use of the Mahalabonis-Distance (cf. [60]) to classify failure modes. For RUL prediction, a NN is employed, achieving 84 % forecasting accuracy. However, the study does not provide details on the extent of the prediction horizon. As before, the authors emphasise the difficulties when selecting appropriate EOL thresholds for respective EMR-DIs. In [100], the authors address previous mentioned issues, whilst emphasising the non-linearity of the degradation process. Based on RT a novel EMR life forecasting strategy is proposed, allowing a prediction horizon of up to 500 actuations ahead. An ensemble of Empirical-Mode-Decomposition in combination with improved Variational-Mode-Decomposition is proposed to decompose RT time-series. Derived features are used as input to a multi-layer NN to predict the trajectory of RT. The authors demonstrate that using the proposed preprocessing steps to prime the input features for the NN can improve model performance. Though, as reported in previous works, the purpose of accurate prediction of an DI trajectory is subject to discussion as it is prone to fluctuations and high levels of variance. Accurately predicting such fluctuations does not support EMR-RUL prediction. This underpins the need for uncertainty quantification with any EMR-RUL estimation methodology as recognised by the authors. [9] propose a method for PdM as well as for the reduction of test-time of railway EMRs. CR and CT are obtained from accelerated life cycle tests at various elevated temperature levels in order to shorten the required time-to-failure. Two physical models are derived to describe the CR increase attributed to contact corrosion and the changes in recorded CT. The models are fitted to life cycle data using the Least-Square-Method and used to evaluate the EMR lifetime at lower temperatures, yielding a low prediction error against the observed EMR life.

E. AUTOMOTIVE EMR

[12] identifies useful DIs for automotive EMRs as CR, PT, ST, BT, AT, and RT. The authors emphasise the non-stationary degradation behaviour of the EMR motivating the choice of NN, due to its capability of learning non-linear relationships, cf. [100]. The performance with different NN architectures and training sets to predict the EMR-RUL is evaluated. The failure mode of the tested automotive EMR is not specified. In [89] an alternative model to predict EMR life in automotive applications is proposed, using the Improved-Fireworks-Algorithm Grey-NN - a swarm optimisation based algorithm. The method is evaluated with life cycle tests at different temperatures predicting the EMR-RUL based on the initial state of the EMR. The authors stress that the model

could be further refined if more parameters would be considered e.g., the operating environment.

F. NUCLEAR EMR

In [8] an embedded non-intrusive online health monitoring method to determine welded EMR contacts from CC waveform in safety critical application e.g., nuclear power plants is presented. The authors demonstrate that welded contacts prevent the EMR armature from moving altering the distinct CC waveform characteristics during de-energisation and re-energisation. It is determined that the distinction between welded and non-welded contacts based on the shape of the CC waveform is possible without requiring the EMR contacts to open. The authors are aware that the application of the proposed method heavily depends on the type and design of the EMR. An integrated circuit for online diagnostic of EMR contact welding detection referred to as *Relay-Output-Card* expands this work in [101]. Similar research has been conducted by [102]. The authors extend on the non-intrusive contact welding detection proposed by [8], [101]. A range of failure criteria aiding the automatic detection of contact welding is reviewed and the robust determination of a healthy CC waveform using an embedded circuit is further improved.

G. STORAGE OF EMR

The degradation of EMR storage, in particular the degradation of the contacts during storage, has been subject to an evolving field of research over the past decade [87], [103]–[108] and [92], [109]. In [103], the authors subject aerospace EMRs to accelerated degradation testing under elevated temperature conditions. It is shown that EMR subjected to temperature stress during storage exhibit a faster increase in CR. This behaviour becomes significant beyond 100 $^{\circ}C$. The authors identify temperature accelerated corrosion as a root cause for high CR and low conductivity, due to surface film formation of oxide corrosion films in silver based contacts. These effects are further analysed in [107], [108], attributing the increase of CR during extended storage time not only to oxides but also to sulphides and carbides depositing on the contact surface. The authors demonstrate that measurements of PT, RT, OT, and BT exhibit distinct trends [103]. Exploiting these findings, a method to predict CR for EMR in storage is developed [104]. The selection of Grey-NN as prediction model is motivated by the non-linearity of the degradation process, cf. [12]. Grey-Theory reduces the effects from fluctuations in the DI on the overall trend. The proposed, combined Grey-NN is superior to using either Grey-Theory or NN. A similar approach, employing Grey-NN for aerospace EMR in storage is presented in [106]. However, instead of CR, CT is the predicted DI. In [105], the authors link the previous research of elevated temperature testing to storage life prediction at ambient temperature. In [87] the authors develop a degradation model for aerospace EMR using PT as DI. PT exhibits a direct linear relationship with the spring force relaxation. Based on the Larson-Miller model a method is proposed establishing the relationship between spring-force decrease and EMR storage life. Though, no assessment is provided, whether the decrease in PT and the failure threshold based on CR resemble similar trajectories for the sampled EMR population i.e., the question for EOL-threshold selection is left unanswered. [92] presents a method to predict EMR degradation during storage based on CR increase. Using Particle-Filtering the unknown parameters of a physical-model are determined from experimental data. Extending on their initial work, the life shortening effects of increased fretting corrosion due to elevated temperature are considered affecting the estimate of the remaining storage life, which is based on trend prediction of CR [109]. As the results indicate, the proposed model is capable of forecasting the storage life accurately. The forecasting performance improves closer to the actual EOL.

H. COMPARISON OF REVIEWED LITERATURE AND IDENTIFIED CHALLENGES

In Table 3 an overview of the reviewed literature is presented, comparing various approaches and objectives to diagnose the operating state of the EMR in order to forecast the EOL or a DI trajectory.

From above analysis various challenges in monitoring and maintaining EMR using data-driven techniques have become evident. Classical DIs do not generalise across different EMR designs, contact types, contact material, operational environments or loading scenarios as each applications results in distinctly different degradation trajectories e.g., [7], [9], [56], [59], [60], [100]. In addition, different failure modes cause classical DIs to exhibit incoherent, opposing trends often even changing within the same batch of components e.g., [6], [60]. This poses a challenge if those DIs are used as direct performance metrics. Predicting or forecasting the trajectory of such DIs is flawed as they are subject to high levels of variance and fluctuations in the switching process e.g., the build up and destruction of oxide films on the contact surface - especially CT and OT - as adverted by the above review. Further, CR is disregarded as DI for a wide variety of EMR as it typically does not exhibit any clear trend or is subject to significant fluctuations e.g., [7], [55]. Research is further challenged by the lack of sufficient amount of EMR life cycle data sets to validate and benchmark the proposed data-driven approaches. Lastly, uncertainty of the forecast is not considered in the reviewed approaches. The listed challenges impede the development of general valid solutions for EMR-SOH or -RUL estimation.

IV. METHODOLOGY

This section presents the EMRUA-Pipeline and formulates the problem of RUA prediction for EMR. However, first the principles of TCN are detailed.

A. PRINCIPLES OF TEMPORAL CONVOLUTIONAL NETWORKS

Proposed by [35], Temporal Convolutional Network (TCN) is a novel, autoregressive DL architecture incorporating

TABLE 3. Summary and comparison of reviewed methodologies.

No.	Ref.	Year	Signals	Features	Method(s)	Objectives
	General DC-EMR					
0	[85]	2004	CV, CI	CR	ARIMA, Exp. Reg. Model	Predicting EOL based on CR trajectory.
1	[10]	2004	CV, CI	DCR, CR, max.-CR, BT	Reg.-Model	Predicting CR.
2	[5]	2006	CV, CI	DCR, CR, max.-CR, BT	Fuzzy Model	EMR contact reliability evaluation.
3	[6]	2010	CR, CC, CV	PT, CT, BT	Reg.-Model	Improving EMR reliability estimation.
4	[88]	2012	CC, CV	BT	Symbolic-Sequence-Analysis	Estimating entropy of BT.
5	[58]	2012	CV, CI	CR, OT, RT, CT, BT, AT, Fluctuation Coefficient	Wavelet-Dec., Linear-Model, Physical-Model	Predicting the DI trajectory.
6	[96]	2017	CV, CC	CV, CC	Weibull-Distribution	Classifying EMR state based on distribution of CV and CC measurements.
7	[60]	2017	Simulation	PT, OT, CC, Spring Force	Mahalanobis-Distance	Classifying EMR failure modes.
	Aviation & Aerospace EMR					
8	[7]	2009	CC, CV	PT, OT, RT	Wavelet-Dec., ARIMA	Predicting EOL based on DIs.
9	[11]	2014	CR	CR	Kalman-Filter, Physical-Model	Contact degradation modelling based on CR.
10	[55]	2015	CV, CR	CR	Grey-System-Theory	Predicting EOL based on CR.
11	[98]	2016	CV, CI	CR	Polynomial-Model	Predicting EMR life based on initial measurements of CR.
12	[97]	2016	CV, CC	CR, RT, ST	Wavelet Dec., Reg.-Model	Predicting EOL based on DIs.
	High-Voltage-DC EMR					
13	[91]	2016	CI	Arc-Charge, Magnetic-Flux	Linear Model	Predicting EOL based on variations in DI.
14	[99]	2017	CI, Erosion Mass, Velocity	Velocity	-	Predicting EOL based on changes in Contact-Velocity.
	Railway EMR					
15	[110]	2016	CV, CC	ST	PCA, NN, Mahalanobis-Distance	Failure classification and RUL prediction.
16	[9]	2018	CR, CV, CC	CR, CT	Physical model	Correlating elevated temperature tests to predict contact degradation at ambient temperature.
17	[100]	2019	CV, CC	RT	NN	Predicting changes in EMR RT.
	Automotive EMR					
18	[12]	2017	CR, CV, CC	CR, PT, RT, BT, ST, AT	Wavelet-Dec. NN	Life prediction utilising the proposed features.
19	[89]	2020	CV, CI	DCR-duration, BT, CV-static, -dynamic)	Particle Swarm Optimisation, Grey-NN	Life prediction based on the initial state of the measured DIs.
	Nuclear EMR					
20	[101]	2016	CC	CC waveform shape	Threshold	Classification of contact welding (cf. [8]).
21	[102]	2017	CC	CC waveform shape	Threshold	Diagnostic circuit to detect the contact welding.
	Storage of EMR					
22	[103]	2012	CR, CV, CC	CR, PT, OT, RT, BT	-	DI derived at elevated temperature, see also [107], [108].
23	[104]	2013	CR	CR	Grey-NN	Predicting the trajectory of CR.
24	[105]	2014	CR	CR	Wavelet-Dec., Exponential-Model	Predicting the trajectory of CR.
25	[87]	2015	CV, CC	PT	Miller-Larson Model	Utilising the linear relationship between spring relaxation and PT to predict EMR-EOL.
26	[106]	2016	CV, CC	CT	Grey-NN	Predicting the trajectory of CT.
27	[92]	2017	CR	CR	Physical-Model, Particle Filtering	Predicting CR.
28	[109]	2019	CR	CR	Physical-Model	Predicting CR.

structural elements from RNN, whilst relying on 1D-CNN. TCN extends the functionality of CNN typically used for e.g., image classification tasks, towards sequence classification and forecasting [111].

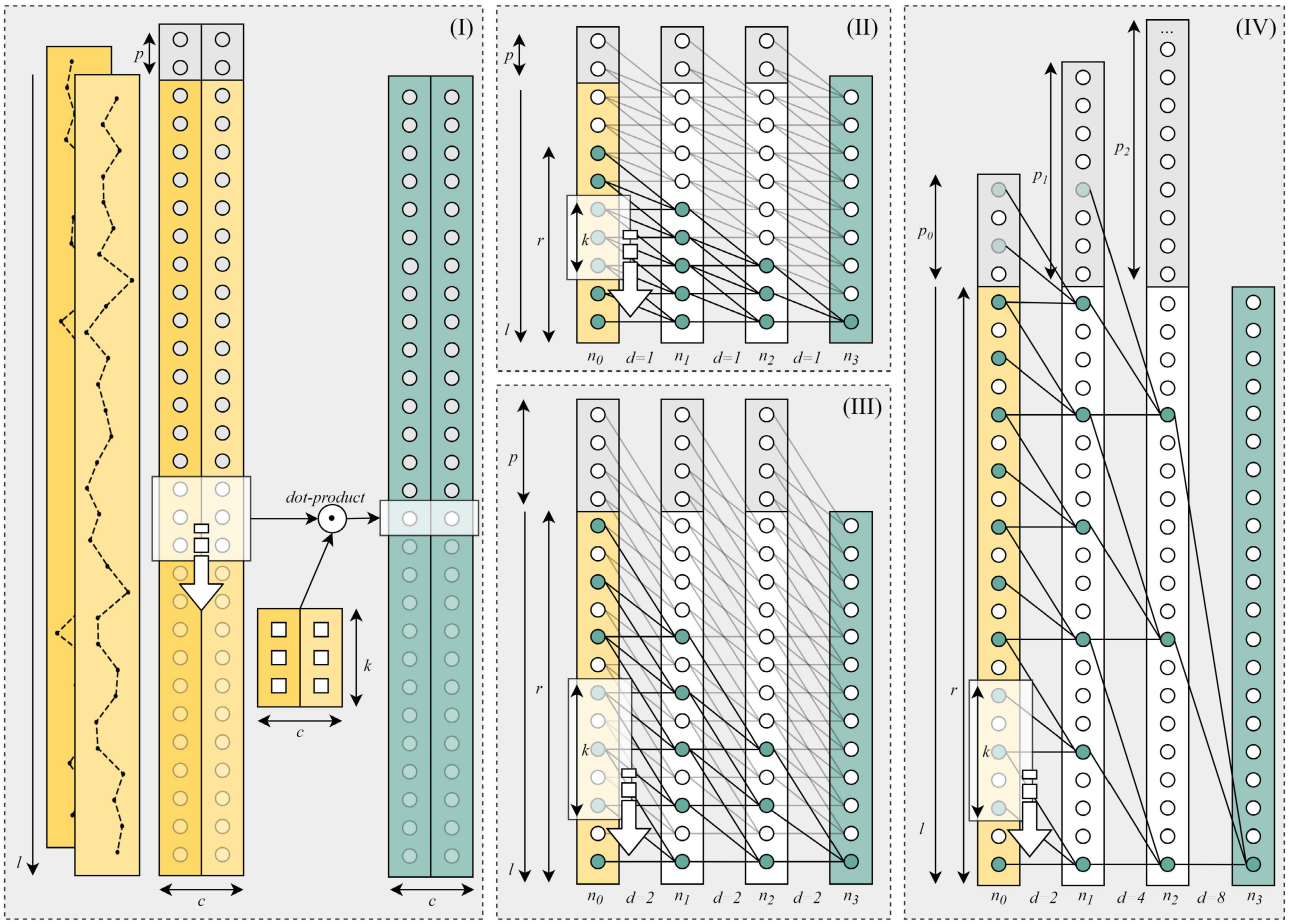

FIGURE 6. (I) Causal 1D casual convolution with multi-channel input $c = 2$ for a sequence of length l and a kernel of size $k = 3$, zero-padding $p = 2$; (II) 1D causal convolution with $k = 3$, $d = 1$, $p = 2$, no full history coverage as $r < l$; (III) 1D causal convolution with $k = 3$, constant dilation $d = 2$, $p = 4$, full history coverage as $r = l$; (IV) 1D causal convolution with $k = 3$, exponential dilation with $d_b = 2$ and $d = [2, 4, 8]$, full history coverage as $r = l$.

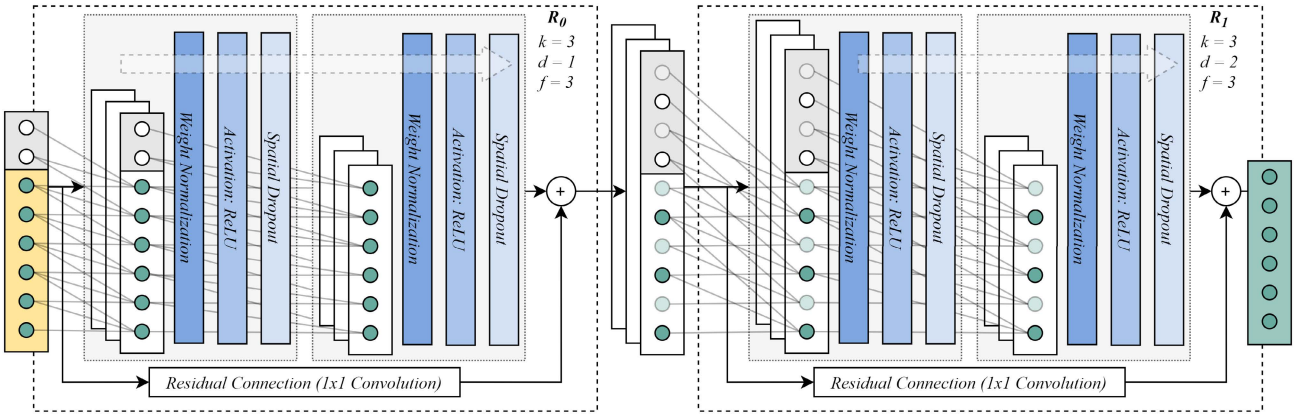

FIGURE 7. A TCN consisting out of two residual blocks $R = [R_0, R_1]$ with filters $f = 3$ and a kernel size of $k = 3$. The first residual block R_0 employs two casual 1D-convolution layers with dilation $d = 1$ and padding $p = 2$. The second residual block R_1 employs two causal 1D-convolution layers with a dilation of $d = 2$ and padding $p = 4$. After each convolution layer, sequentially weight normalisation, activation using ReLU (for non-linearity), and spatial dropout for regularisation are employed. A residual connection is used to stabilise the network during training.

TCN accounts for the caveats of sequence models, compare RNN e.g., LSTM or Gated-Recurrent-Unit Network (GRU) when learning very long sequences [36]. Advantages are the mitigation of the vanishing/exploding gradient problem when back-propagating through time as often encountered with LSTM; reduction of memory usage, training

and inference time over traditional RNN architectures [37]; compared to LSTM, TCN also requires less trainable parameters to store intermediate results [35]. To elaborate, 1D-convolution adopted in TCN shares the learned filters across the entire input feature map of length l per input channel c. This can be attributed to the parallelism of the convolution operation. Given a sequence $x_l = [x_1, x_2, \ldots x_{i-1}, x_i]$, retrieving a result for x_i using RNNs depends on the prediction of x_{i-1} and all previous time steps. However, convolution can operate in parallel on the entire sequence x_l as the same kernel k is shared across the entire layer. Lastly, controlling the size of the receptive field r can be accomplished by different means providing greater flexibility in the design of the architecture [35].

TCN shares the ability to map an arbitrary-length input sequence x_l to an output sequence y_l of the same length using 1D-convolution. However, in sequence modelling it is important that an output y_i only depends on the current and previous inputs $[x_1, x_2, \ldots, x_{i-1}, x_i]$. Fig. 6-(I) displays the principal of so called causal convolution. In case of a multivariate input sequence $X = [X_1, X_2, \ldots, X_c]$, the input feature map is convolved moving a different, learnable kernel of size $k = 3$ for each channel c in one direction, along one axis only across the input sequence. This outputs a 2D tensor $\hat{X}$ of the same length l and width c. The learned kernel of size k is shifted across the input with a step-width of $s = 1$ utilising the same kernel weights for each input channel in each convolution layer. In practice, if $c > 1$, the 1D-convolution can be imagined like a 2D-CNN, where the filters are restricted to the channel. The number of weights used in the model depends on the kernel size k, the number of filters f and the network depth n. As one can see in 6-(I), in order to retain the same sequence length for the output y_l, zero padding at the beginning of the sequence is required. In the case of simple 1D causal convolution the padding length is $p = k - 1$.

The receptive field r, that is the number of elements in the input x_l, which relate to an output y_i, is important to consider. In the case of TCN, the width of r defines how far back the model's horizon reaches. If r covers the entire input length it is termed *full history coverage*. As one can see in Fig. 6-(II), the receptive field r grows linearly with the network depth n as $r = 1 + n * (k - 1)$ if k is constant throughout the entire network. Therefore, increasing r can be achieved by either increasing the depth of the network n or the kernel size k. Hence, due to this linear relationship between network depth n and receptive field r, achieving full history coverage for sequences where l is large would require very deep networks. In turn, this would cause problems with the vanishing gradient and lever the advantages of TCN over RNN based architectures.

To circumvent this problem dilation is introduced. Dilation, somewhat similar to the step-width used in CNN, spreads out the kernel across the input skipping certain elements depending on the dilation step-width d. A kernel of size $k = 3$ and dilation $d = 1$ would convolve over an input of $l = 3$. Contrary, if $d = 2$, the same kernel would cover an input of $l = 5$ with holes at the 2^{nd} and 4^{th} elements. This concept is introduced in Fig. 6-(III). The receptive field grows as $r = n * (1 + d * (k - 1))$, depending not only on n and k, but also on d. However, if d is a constant r still grows linearly. Hence, to more effectively increase r along the network depth, d should grow exponentially as illustrated in Fig. 6-(IV). This yields a dilation of $d_i = d_b^{n_{i-1}}$ and r as per Equation 1.

$$r = 1 + \sum_{i=0}^{n-1}(k-1) * d_b^i = 1 + (k-1) * \frac{d_b^n - 1}{d_b - 1} \tag{1}$$

Typically, the dilation is increased with the base of $d_b = 2$. To achieve full history coverage i.e., $r >= l$, the minimum number of required layers is

$$n = \log_{d_b} *(\frac{(1-l) * (d_b - 1)}{(k-1)} + 1) \tag{2}$$

where the padding for each layer is $p_i = d_b^{n_{i-1}} * (k - 1)$. To avoid gridding i.e., an incomplete coverage of the elements in the input x_l within r, the kernel should be chosen as $k >= d_b$ [45].

Adapted from [112], the authors in [35] utilise a structural element referred to as *residual block* replacing the simple 1D convolutional layer. TCN encapsulates this structural element to improve the stability of the architecture as the model learns a modification of the input feature map [35]. A network using residual blocks R is displayed in Fig. 7 with $d = [1, 2]$, $f = 3$, and $k = 3$ resulting in a network with $R = [R_0, R_1]$ blocks.

The proposed structure alters the typical CNN building block, consisting out of $h = 2$ 1D-convolution layers using the same k and d. The receptive field r which allows full history coverage for this architecture can be expressed as

$$r = 1 + \sum_{i=0}^{n-1} h * (k-1) * d_b^i = 1 + h * (k-1) * \frac{d_b^n - 1}{d_b - 1} \tag{3}$$

$$n_l = \log_{d_b} *(\frac{(1-l) * (d_b - 1)}{(k-1) * h} + 1) \tag{4}$$

After each convolution layer, weight-normalisation to normalise the convolution outputs and reduce effects of an exploding gradient, activation for non-linearity using Rectified Linear Unit (ReLU) and regularisation using channel dropout to minimise overfitting are employed. Contrary to spatial dropout i.e., randomly dropping out some feature maps, channel dropout randomly drops out a set of channels controlled by the dropout rate. To retain the input sequence length l between residual blocks, a residual connection using 1×1 convolution is performed directly on the blocks input and element-wise added to the blocks output. This stabilises the network and counteracts the vanishing gradient problem encountered when back-propagating the errors through deep networks [35].

B. PROPOSED EMRUA PIPELINE

In this section the proposed EMRUA pipeline is introduced. The pipeline performs a set of sequential steps to estimate the EMR's Remaining Useful Switching Actuations (RUA) at any point during the components life. For the sake of clarity - rather than measuring the remaining time to failure as RUL [17], [113] - this work is concerned with the estimation of the number of Remaining Useful Switching Actuations (RUA). RUA refers to the number of EMR making and breaking actuation left, till the EMR is failed due to one of the reasons discussed in Section II-A. Two general stages are considered. *During training and testing*: suitable input feature representations extracted from the raw data are determined; a range of sub-sequence selection strategies to sample from the time-series data are considered; TCN-model combinations for RUA predictions are tuned (the aim is to minimise the loss between target RUA-sequence and estimated RUA-sequence). *During inference*: once the best model has been determined, RUA estimations under consideration of uncertainty can be performed. Fig. 8 provides an overview of EMRUA, cf. Fig. 8-(IV).

1) DATA EXTRACTION

MVTD snippets are recorded during EMR switching. Together, each contact making and the consecutive contact breaking are constituted as one single actuation A. For each actuation A_j from c sensors, a set of sensor signals $X = [X_1, X_2, \ldots, X_c]$ is recorded. The i^{th} signal is $X_i = [x_0, x_1, x_2, \ldots x_s]$ of length s i.e., samples for the contact making and breaking respectively. Fig. 8-(I) illustrates the process of data extraction for the CV and CI. However, one is not limited to these two signals, and other sensors can be considered e.g., the CC. The properties of CV and CI for normally open EMR contacts are detailed in the Appendix C-A and D-A.

2) FEATURE EXTRACTION

The feature extraction process follows a set of consecutive steps, schematically illustrated in Fig. 8-(II). The aim is to derive features which depict the underlying degradation process common among the population of sampled EMR. The mean of a group of l actuations A_j is taken as W_h per extracted feature. We differentiate between two sets of derived features, being time-based reference DIs denoted as feature-set F_T consisting out of c_T features e.g., the BT, AT, RT, etc.; and a feature-set F_S consisting out of c_S features representing a combination out of amplitude-based reference DIs and statistical features, such as the *variance*, *max*, *min*, etc. extracted from CV and CI. Normalisation of the derived feature sets is performed to make them suitable inputs for the TCN. Therefore each feature is scaled to a range of [0, 1] as per Equation 5

$$F_i^{norm} = \frac{F_i - min(F_i)}{max(F_i) - min(F_i)} \tag{5}$$

where F_i denotes the i^{th} feature of the feature set F. In addition to F_T and F_S, we also consider a combination being $F_{T,S} = [F_T, F_S]$. The changes in the waveforms due to deterioration of the EMR from switching under load are presented in the Appendix C-B and D-B. The respective set of features is introduced in Appendix C-C and D-C.

3) SEQUENCE SELECTION

As explained in section IV-A, TCN performs causal-convolution over the input feature map F, to estimate a RUA target sequence of the same length. As the kernel is shared across the entire input sequence, the number of trainable parameters in the model is independent of the sequence length l_s. It only depends on the number of considered input features c, the number of filters f, the kernel-size k, and the number of residual blocks R. However, different strategies can be employed to select a subset of representative windows W from the interval $T = [0, t]$. The different processes of sequence selection are pictured in Fig. 8-(III).

a: GROWING-SEQUENCE INDEXING

This selection strategy of an input sequence of length $l_s = t$, will consider every actuation for the entire interval $T = [0, t]$. Hence, the sequence will grow over the course of life of the EMR till EOL. In practice this poses a challenge as the extension of the sequence length needs to be considered during training. As input to the model serves a randomly selected batch B containing b examples, which vary in their length l_s but remain constant in regard to the number of features c, cf. [114]. However, all sequences within one training batch need to have the same length. Hence, all b randomly selected sequences are padded to the maximum sequence length $l_{s(max)}$ encountered in the batch B, as displayed in Fig. 9. A sequence ranges always from the first switching actuation to an actuation at time t relative to the EOL of the respective sample.

b: LINEAR INDEXING

In the case of linear indexing, the entire degradation sequence is equally considered. $l_s \in \mathbb{Z}^+$ actuations are selected, evenly spaced in the interval of $T = [0, t]$. Hence, even as t increases, l_s remains constant. We can express the selection of l_s actuations as

$$A = \{A_0, A_{\frac{t}{l_i - 1}}, \ldots, A_t\} \tag{6}$$

c: EXPONENTIAL INDEXING

Contrary to Section IV-B3.b, this selection strategy favours recent degradation trends as l_s actuations are selected in the interval $T = [0, t]$, expressed as

$$A = \{A_0, A_{t-(\frac{t^2}{l_i - 1})^2} \ldots, A_t\} \tag{7}$$

4) RUA ESTIMATION

RUA is linear, considering the actuation *passed* against the actuation *left* till the EOL. Equation 8 defines RUA for the i^{th} actuation a_i,

$$\text{RUA}(a_i) = a_{\text{EOL}} - a_i \quad \text{where} \quad a_i \leq a_{\text{EOL}}, a_i \in \mathbb{Z}^+ \tag{8}$$

However, as the TCN is capable of mapping each input $X_{[1,i]}$ to an output $Y_{[1,i]}$, the problem at hand considers a

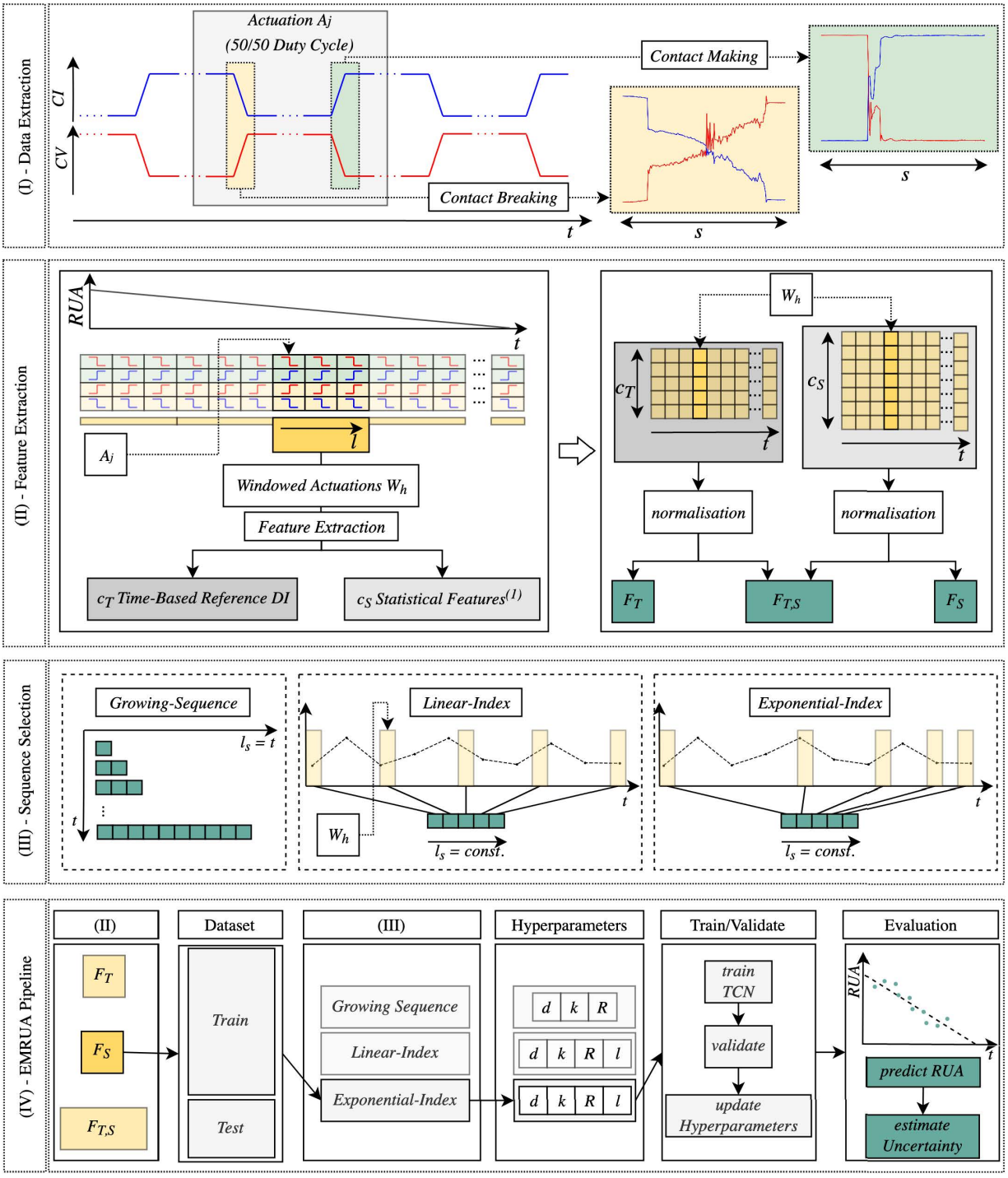

FIGURE 8. **(I) The sampling strategy for CV and CI from the EMR opening and closing waveform during switching; (II) the process of feature extraction and preparation as TCN input feature map; schematic display of the three sequence selection strategies GI, LI and EI; (IV) the EMRUA pipeline. (1) The extracted statistical features are detailed in the Appendix C-C and D-C.**

sequence to sequence mapping task. Hence, RUA can be considered as a vector, cf. Equation 9.

$$\mathrm{RUA}(a_{[1,i]}) = a_{\mathrm{EOL}} - \begin{bmatrix} a_1 \\ a_2 \\ \vdots \\ a_i \end{bmatrix} \tag{9}$$

All prognostics related applications addressing RUL are inevitably concerned with the uncertainty of the forecast. Hence, uncertainty needs to be explicitly addressed in order to provide a verifiable, robust diagnostic or prognostic method [17]. This becomes especially important, if DL approaches are selected as they are considered to be *black-box* models [115]. Sources of inherent uncertainty stem from

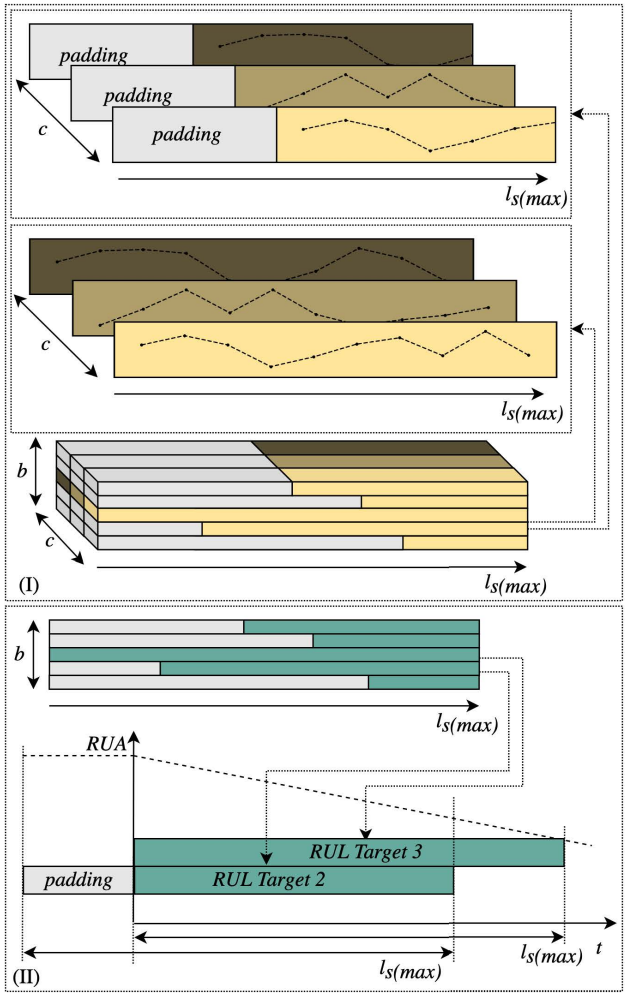

FIGURE 9. (I) The input batch B of batch-size $b = 5$ with a maximum sequence length $l_{s(max)}$ and features $c = 3$; (II) the RUA target sequence for each instance in the input batch.

production variance within the same type of monitored system or component as well as the unknown exact operational conditions. Equally, uncertainty induced by measurement errors should be considered. Selection of appropriate sensors can reduce this type of uncertainty [17]. Beside sensor noise, measurement errors and uncertain state estimations, the future loading pattern might be unknown. Additionally, uncertainty from modelling errors and selection of model parameters has to be considered. One might be able to reduce model uncertainty by increasing the sample-size.

Monte-Carlo Dropout (MCD) can be used to determine uncertainty during inference in DL. MCD has been proposed by [49]. MCD approximates the Bayesian Gaussian Process, providing a highly computational efficient solution for DL to estimate the posterior distribution [48]. The effect of the model's input dimension on the computational complexity is an important aspect to consider [17]. The number of used features during inference has a neglectable effect, however, the length of the input time series might be of concern in terms of computational efficiency as well as full history coverage.

MCD achieves uncertainty estimation by utilising dropout during inference on the trained model f, which results in a different prediction of $Y_t = [y_0, y_1, \dots y_t]$ for an input sequence $X_t = [x_1, x_2, \dots, x_t]$ at each forward pass as the dropout-mask δ^i is selected at random, yielding:

$$Y_t^i = f(X_t|\delta^i) + \epsilon \tag{10}$$

where $\epsilon \sim \mathcal{N}(\mu, \sigma^2)$ represents the Gaussian distributed process noise stemming from e.g., measurement errors. The distribution derived from averaging over N forward passes is somewhat similar to an ensemble of N trained models. One can compare this to estimating a distribution of the learned weights per layer which can be approximated using a relative small number of forward passes i.e., $N \leq 1000$ [50]. To facilitate MCD, [116] suggests to employ dropout after each layer. [48] points out it is important that the dropout rate is kept constant and not tuned during training.

Making use of a batch B with the size b (i.e., the number of passed feature maps) during inference, we can effectively forecast the RUA for N forward passes in parallel so that $b = N$, where each feature map X_t in B is the same input, resulting in a total input $B_t = [X_t^0, X_t^1, \dots X_t^b]$. This allows us to estimate the posterior distribution of Y_t in parallel as the dropout mask $\Delta_N = [\delta_0, \delta_1, \dots, \delta_b]$ for each X_t^i is chosen at random across the input B_t. Therefore Equation 10 can be amended to

$$Y_t^N = f(B_t|\Delta_N) + \epsilon \tag{11}$$

The process is illustrated in Fig. 10. It is evident that DL methods deploying convolution are especially well suited architectures for using MCD to quantify uncertainty, due to the parallel computing capabilities exhibited by those architecture. However, one should be careful with a combination of very long sequences and a large N as this requires significant memory overhead, due to the size of the input feature map.

The RUA is estimated from Y_t^N, as summarised in Fig. 10. The best linear fit for each predicted RUA sequence Y_t^i is determined reducing the residual sum of squares. The *mean* as in Equation 12 and the *variance* as in Equation 13 for each a_i is then calculated from the N extrapolated linear RUA trajectories - ranging from a_0 till the a_{EOL} - to derive a confidence interval. Within this interval the model is 95% confident that the true mean of the population i.e., the true RUA, is contained.

$$\mu(a_i) = \frac{1}{N}\sum_{j=0}^{N} m_j(a_i) + b_j \tag{12}$$

$$\sigma(a_i)^2 = \frac{\sum_{j=0}^{N}((m_j(a_i) + b_j) - \mu(a_i))^2}{(N-1)} \tag{13}$$

C. MODEL CONFIGURATION AND SCORING

An overview of the model hyperparameters is provided in Table 4. The model consists out of a number of stacked residual blocks, depending on the final width of the receptive

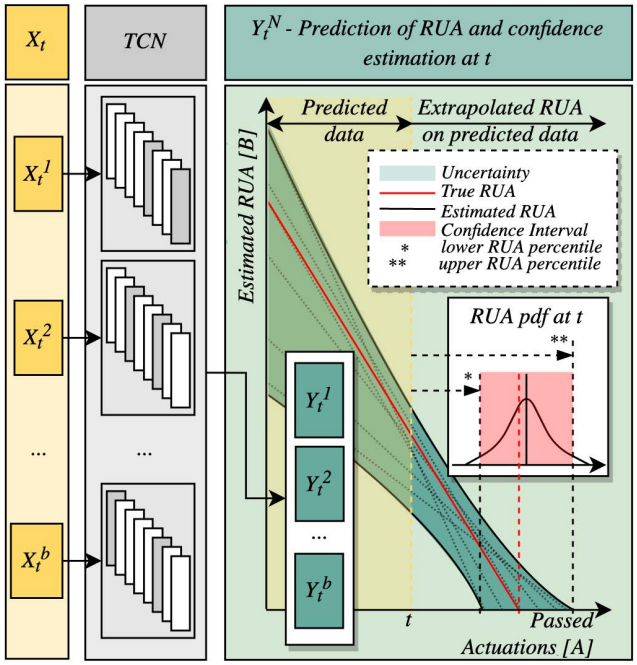

FIGURE 10. Parallel sampling of RUA from an input X_t using a batch B with b different dropout masks during inference, predicting Y_t^N posterior RUA sequences.

TABLE 4. Evaluated TCN model hyperparameters.

Hyperparameter		Value
Filters	f	64
Kernel	k	[3, 5, 7]
Dilation base	d_b	[2, 3, 4]
Residual blocks	R_n	[6, 7, 8]
Dropout rate	-	0.5
Activation	-	ReLU
Optimisation	-	Adam
Learning Rate	-	0.0001
Batch size	b	[400, 200, 100]
FC-Layer Units	-	1
FC-Layer Activation	–	Linear

field r; followed by a final FC layer using linear activation. Dropout is employed within each residual block. Model performance is evaluated using Mean Absolute Error (Mean Absolute Error (MAE)), Mean Absolute Percentage Error (Mean Absolute Percentage Error (MAPE)) and Root Mean Squared Error (Root Mean Squared Error (RMSE)) where RUA_i denotes the target and RUA_i^* the estimated RUA.

$$\mathrm{MAE}(\mathrm{RUA}_i^*, \mathrm{RUA}_i) = \frac{1}{N}\sum_{i=0}^{N} |\mathrm{RUA}_i^* - \mathrm{RUA}_i| \tag{14}$$

$$\mathrm{MAPE}(\mathrm{RUA}_i^*, \mathrm{RUA}_i) = \frac{100\%}{N}\sum_{i=0}^{N} \frac{|\mathrm{RUA}_i^* - \mathrm{RUA}_i|}{\mathrm{RUA}_i} \tag{15}$$

$$\mathrm{RMSE}(\mathrm{RUA}_i^*, \mathrm{RUA}_i) = \sqrt{\frac{1}{N}\sum_{i=0}^{N} (\mathrm{RUA}_i^* - \mathrm{RUA}_i)^2} \tag{16}$$

In addition to the RMSE, a scoring metric proposed by [117] is adopted to evaluate the performance under consideration of the models' estimated uncertainty, cf. for a prognostics use case [23], [118]. An accuracy zone α is defined providing bounds of allowed deviation from the targeted RUA limited by an upper threshold α^+ and a lower threshold α^-. α is selected according to the needs of the specific application. Here, $\alpha = 0.2$ is chosen for evaluating the EMRUA. The α_{sc} is calculated by counting the frequency of RUA estimates within the $\alpha^{\pm}$ bounds, cf. [117], [119].

V. EXPERIMENTS AND RESULTS

This section discusses the design and results of the EMR life cycle experiment. Furthermore, the results of the EMRUA are presented.

A. EMR LIFE CYCLE EXPERIMENTS

As previously stated, the contacts of EMR are most liable to failure, hence the EMR life is - in most cases - determined by the contact life or so to speak the electrical life. In comparison, the mechanical life of the EMR is significantly higher [1]. Therefore, the focus of the life cycle experiments are contact related failure modes. To understand the factors affecting the EMR contact life, a Design of Experiment (DOE) provides statistical control to select the test parameters under consideration of the operational thresholds. In particular, when testing EMR it is important not to induce uncharacteristic failure modes through poor choice of test-parameters. Hence, a popular approach to test only the contacts is a *model switch* i.e., a device which allows to precisely control the switching parameters [120], [121]. However, whilst yielding results applicable to the contact material, carefully tuning such replica to match the properties of an EMR under test is challenging [1]. Factors such as closing velocity of the contacts, bounce, etc. need to be considered. Further guidance and considerations in regard to EMR life cycle tests is provided in the Appendix B.

As one can see in Fig. 11-(I) the experimental setup relies on a National-Instruments PXIe8880 controller for data collection operating with LabVIEW-RealTime and monitored on a separate Control-PC. In combination with the Real-Time controller a PXI-2567 module is used to precisely trigger switching of the EMR under test. Experimental data is collected using the PXIe-6365 module at a sample rate of 25 *kHz* for CV, CI and CC. Sampling starts prior to, and ends after each making and breaking actuation respectively. The interval in between an actuation is not recorded, cf. Section IV. CC is directly recorded whilst the amplitude of the CV signal is reduced using a voltage divider prior, due to the limited voltage range of the measurement hardware. Lastly CI is recorded with a hall-effect current sensor. As shown in Fig. 11-(III) all recorded data is then streamed to the Control-PC. To facilitate CR-measurements, a secondary circuit can be switched

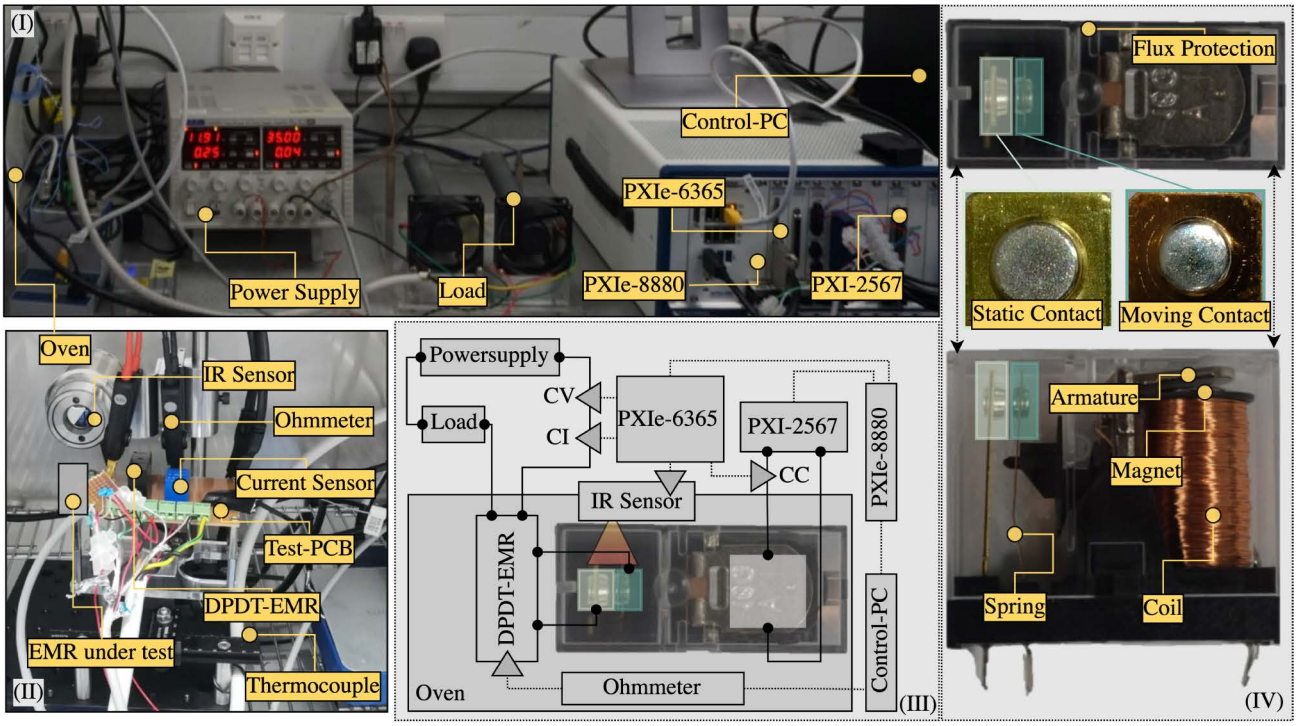

FIGURE 11. (I) Overview of the developed EMR life cycle test platform. The power supply is directly connected to the Control-PC to allow for an automatic setup of the test parameters. (II) The EMR test-PCB is situated in the oven and allows quick exchange of the test-sample. The infrared sensor (IR), and the Ohmmeter (4-Wire-Measurement) are placed in the oven as well. (III) A simplified schematic of the test-setup using the PXIe-8880 module to collect and stream data to the Control-PC. This allows deterministic control of the experiment using LabVIEW-RealTime. (IV) The tested EMR, top- and side-view of coil and moving armature, static contact carrier and the silver-plated contact rivet, the moving contact carrier realised as contact spring.

in using a Double-Pole-Double-Throw (DPDT)-EMR positioned as close as possible to the EMR under test. This circuit is connected to the Ohmmeter *4-wire* measurement setup which is in turn directly linked to the Control-PC. CR measurements are taken at regular intervals. Therefore, switching of the contacts is paused, the EMR under test is then closed. The DPDT-EMR - controlled via a secondary channel on the PXI-2567 - switches from the test-circuit to the CR-measurement-circuit. Simultaneously, using an infra-red temperature sensor the EMR casing temperature is recorded in close proximity to the EMR contacts. A dedicated PCB has been developed to house the necessary sensors and components and facilitate the exchange of the EMR under test, once failed. The test-PCB is shown in 11-(II). It is placed in an oven to control the operating temperature. The ambient temperature within the oven is monitored as reference. An external power supply in combination with two parallel, variable resistors set up with opposing winding to reduce effects of load inductance is used to provide a nearly resistive test-load. This setup is displayed in Fig. 11-(I). The interested reader is referred to [52] for further considerations of this experiment.

The tested component is displayed in Fig. 11-(IV). A general-purpose Single-Pole-Single-Throw-Normally-Open (SPST-NO), unsealed EMR has been selected as test component. Its specifications are listed in Table 5.

TABLE 5. Test EMR specifications.

Parameter	Specification
Coil Rating	5 VDC, 105 mA
Operate/ Release	at max. 70%/ min. 15%
Contacts Rating	30 VDC, 10 A (resistive load)
Contact Resistance	$30m\Omega$
Contact Type	Plated Copper Rivets
Contact Plating	$AgSnO_2In_2O_3$
Max. op. Temp.	$70°C$
Casing	Flux-Protection

B. CONDUCTED EXPERIMENTS AND OBSERVED FAILURE MODES

EMR life cycle experiments have been conducted at 30 VDC, 6 A, 0.25 Hz switching frequency, 50 % duty cycle and 60 $°C$ ambient temperature. All tested EMRs were subjected to the same failure mechanism: prior to failure, various contact-sticking events occurred, whereas continuous material loss due to electrical erosion led to diminishing contact material thickness. Combined with a reduction in contact over-travel and spring-force due to ageing, an increase in poor contact making - as the effective contact area is continuously reduced - resulted in strenuous heat accumulation within the contact carriers and contact rivets. The parting velocity of contacts decreased and bounce duration increased, cf. Appendix C, Fig. 21 and 23. Such alterations in the

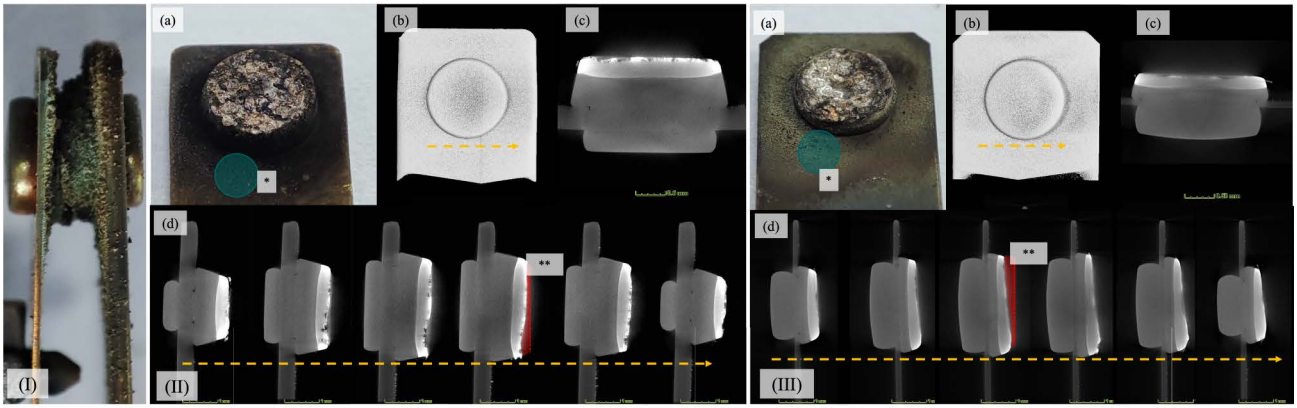

FIGURE 12. (I) Example of stuck-closed EMR contacts (unsealed), due to contact welding; (II) (a) photography of the static contact carrier (anode) after failure; (b),(c) and (d) CT-Scans and cross-sections (the brighter coloured grey area on the contact rivet is oxidised silver and the silver contact plating material, while the darker grey area is the copper contact rivet body); (*) sputtered, eroded contact material; (**) dashed red line represents the contact height of the new EMR contact; (III) photography and CT-Scan of the moving contact carrier (cathode) after failure, cf. (II).

switching pattern favour micro-welding between the contacts, which manifests in an increasing number of contact sticking events towards the EOL. Further, bouncing duration lengthens, with an increasing duration between the bounce events, whilst bouncing intervals shorten. Late, short bouncing events increase the likelihood of contacts to close directly on the molten surface and small welds to harden prior to rupture from the next bounce [71], [75]. Ultimately the contacts weld during bouncing whilst contacts close. The strength of the weld exceeds the spring force of the reverting contact carrier. The EMR is subjected to a *stuck-closed* failure. As further indication of an imminent failure the contact temperature can be considered. Appendix A, Fig. 18 depicts the changes in EMR casing temperature, whilst the ambient temperature is kept constant, recognising a clear upwards trend in the last third of the EMR life following a relative stable phase. The heat build-up can be attributed to a set of interrelating mechanisms. The increased AT is the most significant contributor, cf. Appendix D-C, Fig. 27. Another factor contributing to contact degradation, accelerated by the increasing heat dispersed from the electrical arcing, is a reduction in stiffness of the moving contact carrier. Hence, a reduction in contact force and contact velocity is to be expected, relating to an increasing AT. Accelerated heat-build is promoted by the design of the EMR under test as the moving contact carrier is significantly thinner than the static contact carrier, cf. Fig. 11-(IV).

Analysis of the stuck-closed EMR contacts provide further insights into the failure mode and mechanism. Fig. 12-(I) shows an example of welded contact rivets. Sputtered contact material is distributed around the contact rivets, consisting out of partially oxidised contact plating material and carbons.

Fig. 12-(II) and 12-(III) show cross-sections of a welded moving and static contact rivet respectively using a CT scan. Both failed contacts exhibit severe damage across the entire contact surface, with a near complete loss of the original plating material and structure. Fig. 12-(I), 12-(II-a-*), and 12-(III-a-*) show the deposition of sputtered black material on the contact carrier surface in the vicinity of the contact rivet. This material consists out of silver-oxides and carbons as EDX analysis suggests. The moving contact carrier displays an increasing material loss towards the upper edges of the contact rivet, but essentially no loss of material towards the bottom of the contact body, cf. Fig. 12-(II-d-**). The static contact on the contrary shows significant loss of contact material towards the bottom. Electrical arcing from the static contact carrier rivet - the anode - to the moving contact carrier rivet - the cathode - is the root cause for the observed distribution of contact material and the concurrent net-loss of material during switching. The craters on the static contact, typical for the anode in a DC setting, can be seen in the cross sections of Fig. 12-(II-d). This is an indication for a relative short duration of the ambient arc, being predominantly in the anodic arc phase as material build-up and pip formation would be expected on the anode with longer duration gaseous-arcs.

C. TCN PERFORMANCE COMPARISON

This section discusses the models' performances, under consideration of the number of trainable parameters, the kernel-size k, the number of residual blocks R, and the dilation-base d_b for the three extracted feature-sets F_T, F_S and $F_{T,S}$. Further the effects of the sequence-selection strategies GI, LI and EI are investigated. The model performance is evaluated on the life cycle of 10 representative EMR test samples subjected to *stuck-closed* failures, cf. [52]. Thus, all displayed results are averaged over the test set unless stated otherwise.

The model configuration in conjunction with the size of the receptive field r affects model performance. Whilst increasing the size of the receptive field r, increasing the kernel-size k or the number of residual blocks R also increases the number of model parameters as can be seen in the bottom of Fig. 13-(I). The model performance does not necessarily

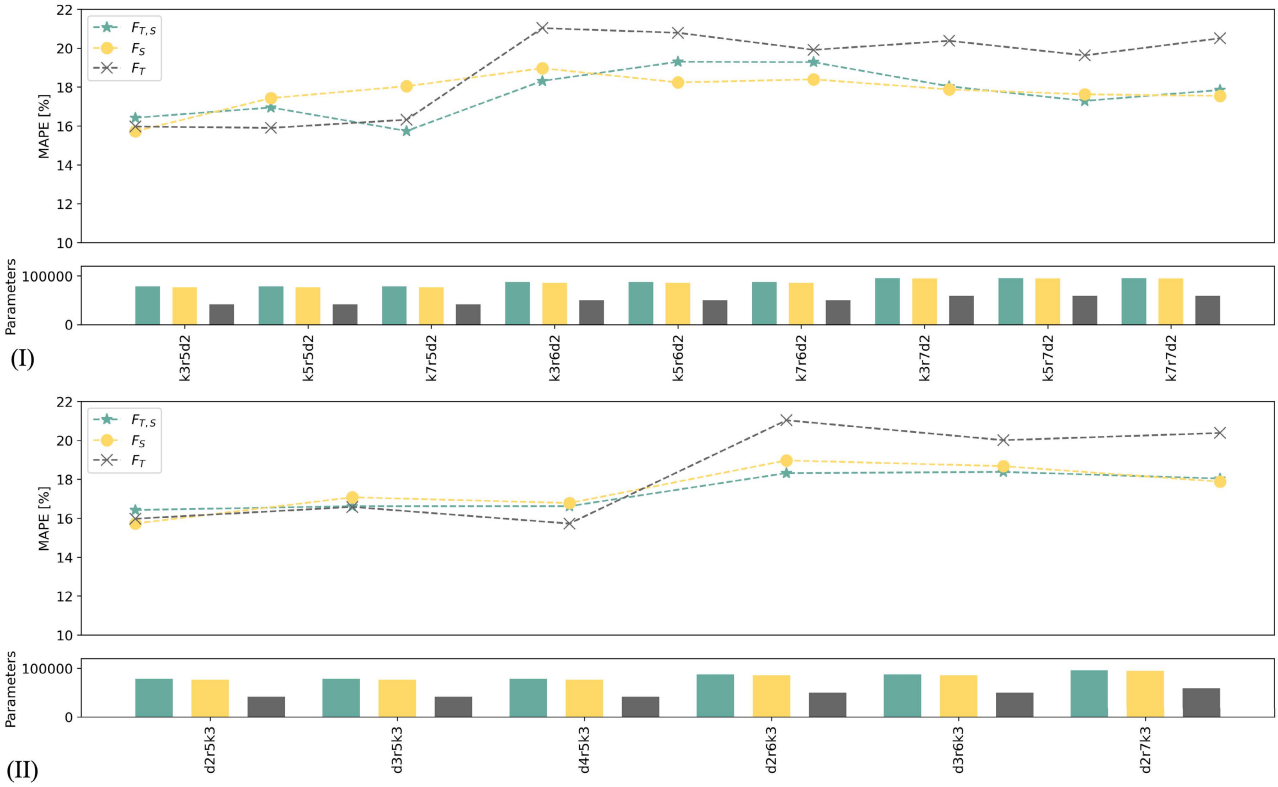

FIGURE 13. (I) Kernel k against Residual-Blocks R, with constant dilation-base $d_b = 2$ for sequence-selection strategy GI; (II) Dilation-base d_b against Residual-Blocks R, with constant Kernel $k = 3$ for sequence-selection strategy GI; average performance on all test samples.

improve with an increase in model complexity. In fact, apparent for data set F_T, an increase of stacked residual blocks R beyond 5 leads to performance deterioration increasing the MAPE respectively. For both F_S and the combined data set $F_{T,S}$, all tested configurations exhibit similar results, though some dependency on the architecture can be recognised.

Altering the dilation base d_b to increase the size of the receptive field r without increasing the number of model parameters does not improve performance, cf. Fig. 13-(II). This might suggest that increasing the receptive field r beyond a certain threshold only improves performance with a parallel increase of trainable parameters. However, care should be taken to avoid overfitting.

As pointed out in the review of related literature in Section III traditional features i.e., time-based reference DIs have been incorporated in the data set F_T. Its performance is displayed in Fig. 14. Across all selection strategies GI, LI and EI performance varies over the tested EMR samples. However, selection strategy EI exhibits less variance. Comparing LI and EI, the prior one exhibits slightly better performance for the model LI-$k = 7$-$d_b = 2$-$R = 6$; model EI-$k = 3$-$d_b = 2$-$R = 6$ yields similar results having considerable less trainable parameters due to the smaller kernel-size ($k = 3$ instead of $k = 7$).

Evaluating the performance of the statistical data set F_S, displayed in Fig. 15 consistent results for the LI and EI

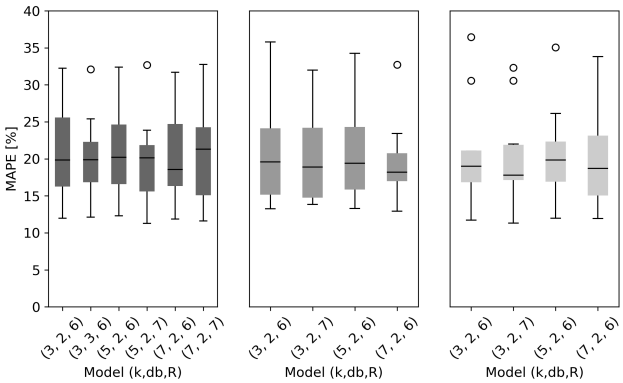

FIGURE 14. Performance results on all test samples of selected model configurations - F_T - Left: GI, middle: LI, right: EI.

sequence selection strategy are achieved reducing the variance in performance compared to F_T. Only F_S-GI exhibits considerable higher levels of variance among all tested configurations compared to F_S-LI and F_S-EI.

Combining the data sets F_T and F_S as a joint feature set $F_{T,S}$ does not generally improve the model performance. On the contrary, adding F_T seems to impair the overall performance in some instances. This can be seen in an increase in performance variance, cf. Fig. 16.

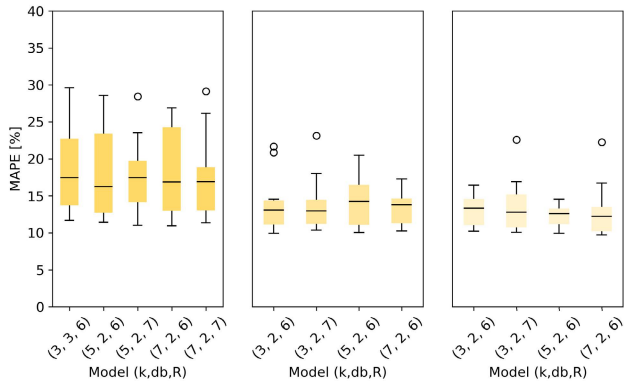

FIGURE 15. Performance results on all test samples of selected model configurations - F_S - Left: GI, middle: LI, right: EI.

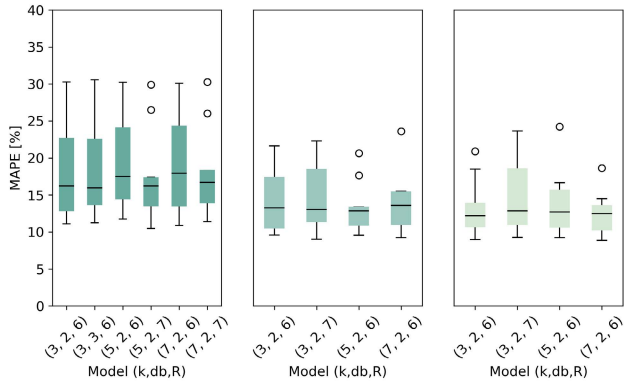

FIGURE 16. Performance results on all test samples of selected model configurations - $F_{T,S}$ - Left: GI, middle: LI, right: EI.

With respect to the results in Fig. 14, 15 and 16, we report performance averaged over all tested EMR samples for different model configurations in Table 6. The best performing model achieves a MAPE=12.39 % using the configuration EI-k = 7-d_b = 2-R = 6 trained on $F_{T,S}$ (87169 trainable parameters). With α_{sc} = 92% the gross of all predictions resides within the $\alpha\pm$ confidence zone. The best performing model using only statistical features F_S is of similar configuration with k = 5 instead of k = 7 EI-k = 5-d_b = 2-R = 6. This model requires slightly less parameters due to the reduced size of the input feature-map and kernel size (85889 trainable parameters). As already demonstrated, in general EI and LI in combination with F_S or $F_{T,S}$ are superior to GI or F_T.

The findings - in terms of the selected feature sets - confirm the challenges of time-based reference DIs in a prognostics scope, pointed out in the literature review, cf. Section II-C. The same type of EMR yields high variance within time-based reference DIs, partially due to fluctuations of e.g. AT, RT, or PT during the fast contact making and breaking. Hence, such features do not necessarily provide the best performance nor robust result. The set of statistical features F_S provides somewhat more stable results among all tested EMR and TCN configurations. Combining F_T and F_S as a joint

TABLE 6. Average results of the best performing models using sub-sampling strategy *S* - EI or LI; sorted ascending to MAPE; *k* - kernel; d_b - dilation base; *R* - Residual blocks; *r* - receptive field; *F* - data set; validation metrics MAE, MAPE, RMSE and α_{sc} with *alpha* = 0.2.

S	k	d_b	R	r	F	MAE	MAPE	RMSE	α_{sc}
EI	7	2	6	757	$F_{T,S}$	144.67	12.39	179.04	0.92
	5	2	6	505	F_S	140.34	12.40	174.38	0.92
	3	2	6	253	F_S	147.70	12.96	183.11	0.90
	7	2	6	757	F_S	154.56	13.07	187.67	0.91
	3	2	6	253	$F_{T,S}$	155.13	13.19	189.80	0.91
LI	5	2	6	505	$F_{T,S}$	157.15	13.33	190.63	0.89
	7	2	6	757	F_S	155.03	13.41	190.72	0.88
EI	5	2	6	505	$F_{T,S}$	162.28	13.71	195.27	0.91
	3	2	7	509	F_S	161.54	13.79	196.88	0.91
LI	7	2	6	757	$F_{T,S}$	164.86	13.85	198.31	0.88
	3	2	7	509	F_S	165.45	13.98	198.47	0.87
			6	253	F_S	165.38	14.02	198.68	0.88
					$F_{T,S}$	169.29	14.31	203.29	0.87
			7	509	$F_{T,S}$	176.26	14.47	210.56	0.87
	5	2	6	505	F_S	171.35	14.58	208.31	0.86
EI	3	2	7	509	$F_{T,S}$	177.19	14.73	210.78	0.91
LI	7	2	6	757	F_T	228.65	19.37	272.52	0.67
EI	3	2	7	509	F_T	229.86	20.11	273.63	0.73
	7	2	6	757	F_T	232.55	20.38	276.90	0.69
EI	5	2	6	505	F_T	229.39	20.54	275.84	0.71
LI	3	2	7	509	F_T	238.67	20.58	285.01	0.68
EI	3	2	6	253	F_T	233.75	20.63	278.30	0.72
LI	5	2	6	505	F_T	245.88	21.22	289.43	0.64
	3	2	6	253	F_T	242.30	21.24	287.28	0.62

feature set $F_{T,S}$ does not reflect a significant improvement. Considering sequence-selection strategies - the performance of GI is worse than LI or EI. This might be attributed to the comparably smaller history coverage of each sequence point of GI selected inputs in TCN. No significant difference in performance between LI and EI can be recognised, suggesting that recent changes in the degradation might not contribute significantly more to the average degradation rate and RUA estimation respectively.

Based on the strategy presented in Section IV, RUA forecasts can support timely decisions for maintenance scheduling. The performance of different sequence-selection strategies and data sets in terms of RUA prediction is illustrated through an example in Appendix A, Fig. 19. The forecasting performance matches our prior findings, where a combination of data sets and the LI or EI sequence selection strategies yield stable results. Again, purely relying on traditional time-based reference DIs might produce misleading results.

In order to evidence the performance gains through TCN, the proposed DL architecture is compared to a reference LSTM model previously employed in RUL forecasting proposed by [122]. The results are displayed in Table 7. TCN significantly improves performance as the feature space increases i.e., using F_S or $F_{T,S}$, despite using less parameters.

Fig. 17 visualises the inference phase of the EMRUA pipeline, which can provide timely RUA estimation in order to be embedded in a maintenance solution e.g., PdM. The RUA and the associated confidence interval is estimated at three different times t during the EMR life. As the true RUA decreases, the model's estimation improves, assured

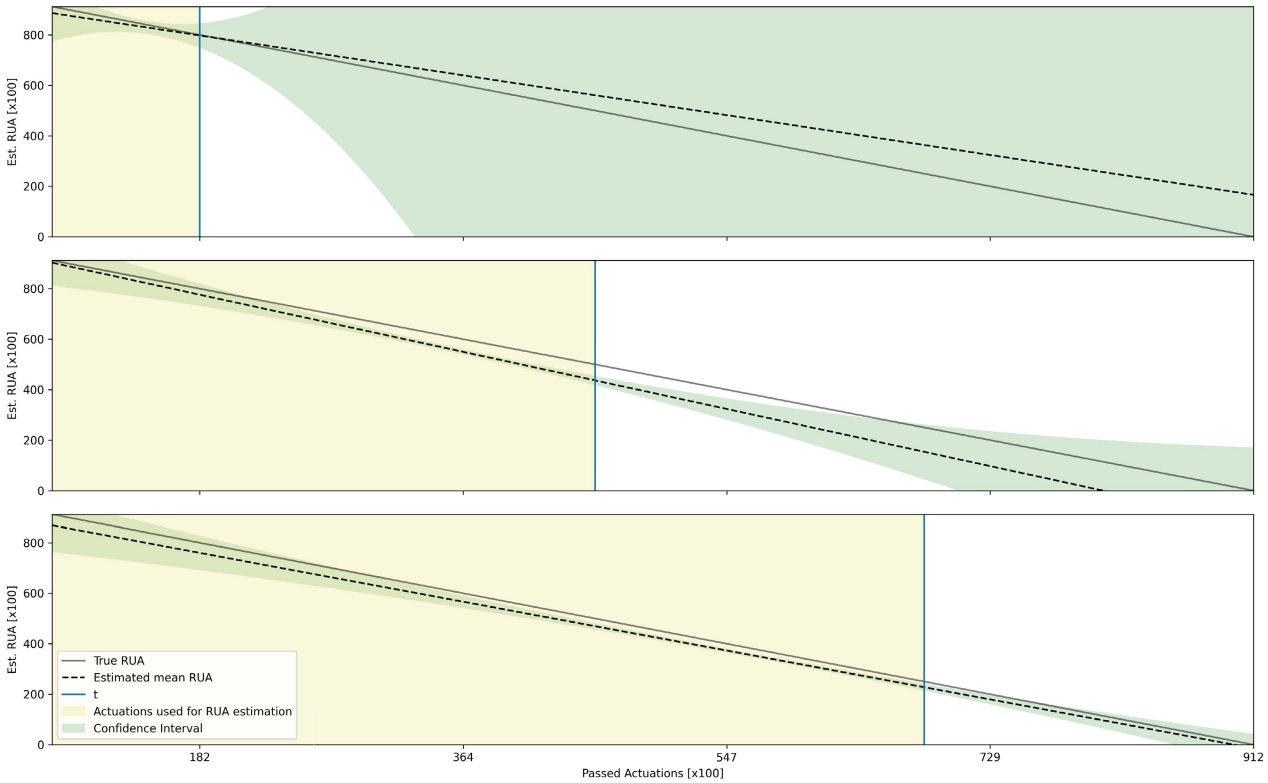

FIGURE 17. Exemplary predicting RUA for one EMR at time t prior to: (top) 80000 actuations till failure; (centre) 50000 actuations till failure; and (bottom) 25000 actuations till failure. The EI sequence selection strategy and the data set $F_{T,S}$ are used.

TABLE 7. Comparison of the best performing TCN and a reference LSTM architecture for the LI sub-sampling strategy.

Model	Data set	Parameters	MAE	MAPE	RMSE
TCN	F_T	50305	228.65	19.36	272.52
	F_S	85889	155.03	13.41	190.72
	$F_{T,S}$	87169	157.15	13.33	190.63
LSTM	F_T	54601	198.47	16.87	230.93
	F_S	165801	223.37	18.84	276.07
	$F_{T,S}$	169801	272.09	21.34	327.13

through narrowing confidence intervals and matching mean RUA prediction.

D. DISCUSSION AND FUTURE WORK

As the above analysis demonstrates, high variance among samples in the data set is present, despite the same failure modes. However, within the limitations of the considered scenario of continuous EMR switching, the proposed configuration of TCN exhibits promising results based on the captured life cycle data. Sources of uncertainty can be further reduced through collection of additional data. EMRUA as a prognostics method can drive PdM, complementing existing EMR maintenance decision making paradigms. It can provide additional confidence in EMR performance, important within critical systems. EMRUA has the capability of efficiently providing real-time insights in the individual EMR health with the associated uncertainty estimate, rather than blindly relying on conventional maintenance measures. EMRUA only relies on CV and CC measurements, which are already commonly collected in many safety critical systems. However, only *stuck-closed* failures were considered. Though, as our literature review has indicated, failure precursors are subject to specific failure mechanisms in turn responsible for different failure modes. Time-based reference DIs are especially liable to such changes and could therefore develop distinctly different trajectories for various failure modes. To what extent this is also the case for the developed statistical DIs contained in the developed feature set F_S is subject to speculation at this point. Thus, training individual models for different failure modes might be necessary and will be subject of future work. In addition, further investigation of the methods' robustness to changes in the volume and granularity of available training data as well as the sampling rate is needed. Optimisation of the hyperparameter selection through e.g. grid search or randomised search should be then considered. Transfer learning is an area of interest, bearing the potential to reduce training time not only among models for different failure modes but also in respect to reducing the amount of training data required when changing the EMR type e.g., a different contact material or design. Of special interest is the investigation of alternative measurements e.g., the contact temperature using an infrared temperature

sensor. Sensing such waveforms and extracting meaningful features could improve the model's performance, though the practicality of such method might be limited. Lastly, we aim to benchmark the concept of EMRUA on various high volume PHM related data sets.

VI. CONCLUSION

EMRs are omnipresent in electrical systems. A data-driven maintenance paradigm has the potential to improve EMR reliability within these systems.

To facilitate the development of a prognostics method, we first discussed the EMR's failure modes (e.g., high CR, stuck-closed and stuck-open contacts) and mechanisms (e.g., electrical arcing, contact welding, contact contamination, fretting) acting predominantly on the electrical contacts. We reviewed and explained the limitations of current practices in EMR reliability modelling - relying solely on traditional time-based reference DIs or CR for determining the EMR SOH and RUL - in regard to their applicability in a data-centric context.

Based on this state-of-the-art analysis, our methodology presents a novel approach including but not limited to EMRs. Our method is aligned to the challenge and opportunities of high volumes of MVTD and efficient monitoring of EMRs. Our proposed DL-pipeline EMRUA utilises the increasing volumes of aggregated EMR data sampled from CV and CI switching waveforms, to provide an accurate RUA estimation throughout the EMR life. TCN has been adopted as autoregressive DL strategy incorporating MCD based uncertainty quantification as a computationally efficient implementation during inference. To support online maintenance decision making, the trade-off between model complexity and model performance were studied. Therefore, the effects of various model hyper-parameters on the predictive performance under consideration of the amount of trainable parameters has been investigated. Additionally, three different feature combinations and subsampling strategies have been explored. The results indicate that TCN achieves the best performance and the lowest forecasting error (MAPE $= \pm 12\%$) using a combination of time-based and statistical features and either EI or LI subsampling. However, it is demonstrated that in some instances classical, time-based reference DIs can have adverse effects on performance. We developed an EMR life cycle test platform to facilitate training, testing, and validation of the EMRUA pipeline through the generation of high volumes of accurate and representative EMR *run-to-failure* data. Further, we addressed the challenge of limited availability of EMR life cycle data in a research context.

Summarising, based on EMR life cycle data we collected, it is demonstrated how TCN can be fused into a prognostic method. The proposed approach emphasises the adoption of DL for PHM, considering high volumes of data. This aids future research utilising DL - in particular for EMR - to develop novel, data-driven maintenance solutions.

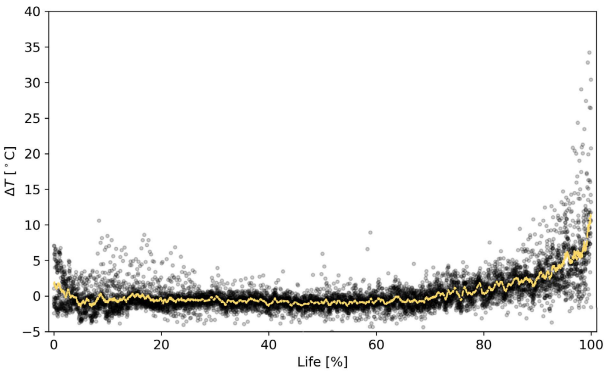

FIGURE 18. Average changes in EMR temperature throughout the EMR life measured with an infrared temperature sensor on the EMR casing.

APPENDIX A
SUPPORTING FIGURES

A. CONTACT TEMPERATURE

Refer to Fig. 18.

B. TCN PERFORMANCE

Refer to Fig. 19.

APPENDIX B
EMR TESTING CONSIDERATIONS

Despite the fact that alterations in CR are not necessarily reliable indicators for EMR wear, it remains a key-measure to judge EMR performance. [57], [123] specify *dry*-contact measurements preferable at low test currents and voltages of less than 80 mV to mitigate effects of electromagnetic-force. *Dry* contact measurements might not return accurate CR measurements if the contacts are under load. Fritting can be the cause for significantly higher CR measurements. The presence of films on the contact surface can relates to this phenomenon. As electrical destruction of the isolating layer can be achieved by switching at higher voltage, an instantaneous change of CR can be observed when increasing the voltage across contacts. The voltage at which this breakdown takes place is referred to as *wetting-voltage*. The initial drop in CR is commonly referred to as *A-fritting*. Its extend depends on the thickness of the insulating layer. The CR then settles on a plateau and the current flows to isolated, scattered *a-spots* creating constricted regions of high current density. In turn a heat up of the vicinity around the current carrying paths thermally destroys the adjacent isolation barrier. This process increases the effective contact area until a sufficiently large contact area is established. Latter process is termed *B-fritting*. In regard to contact testing [1] points out that, though it is industry standard to test at maximum rated specifications, no assurance can be given that the degradation behaviour of electrical contacts at lower loads will be similar. For example, testing using high loads will circumvent problems like contact film contamination encountered only at lower loads.

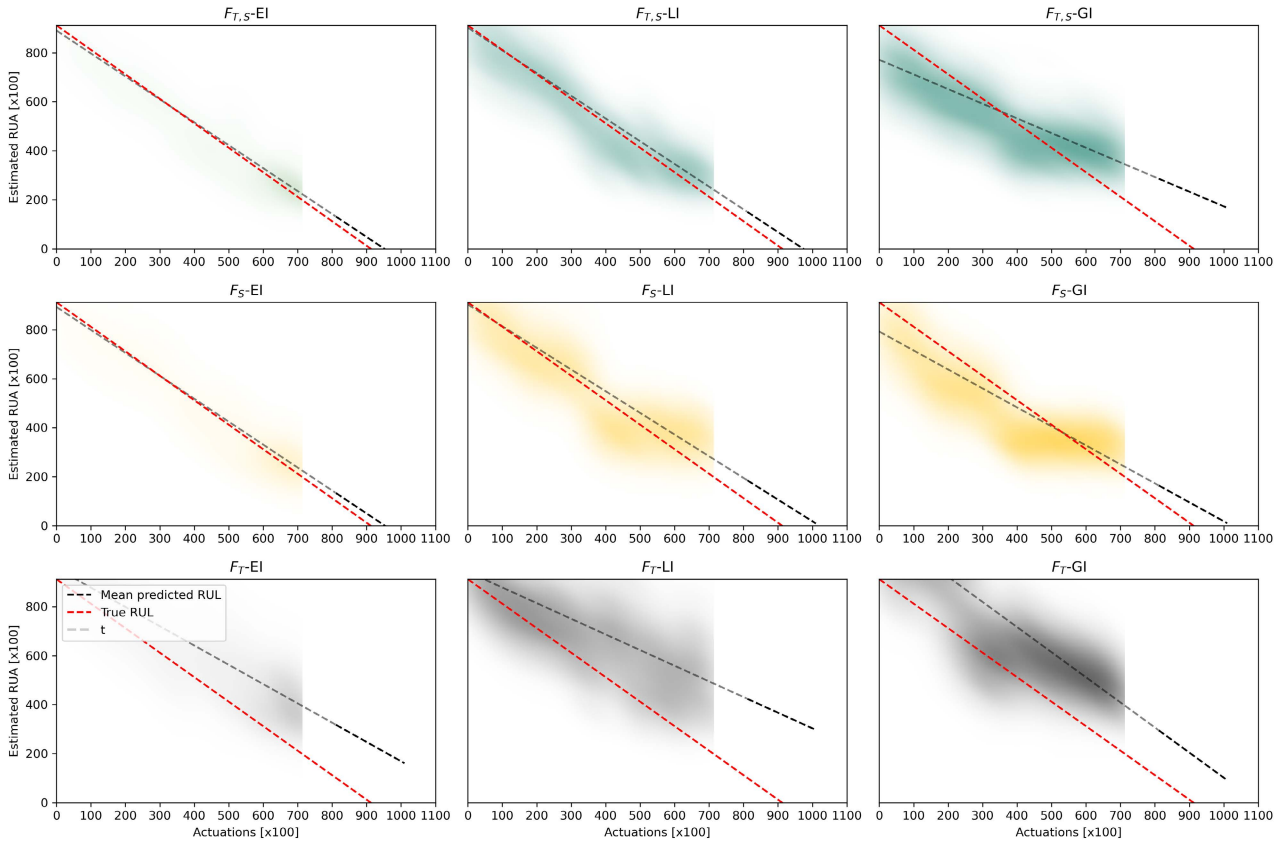

FIGURE 19. Performance of various TCN configurations 20000 actuations before EOL for one EMR sample.

In order to accelerate the general degradation or one particular degradation type, one can explore different means. The most apparent approach is an increase in switching frequency under the assumption that this does not alter the overall degradation behaviour of the contacts and the EMR. Alternatively, an increase of the contacts stress through elevated current levels can be considered. In DC testing, the effects of switching the anode and cathode among the contacts in the test setup alters the degradation pattern as e.g., cost-efficient consumer-EMRs tend to have a thicker stationary contact carrier and a thinner movable contact carrier i.e., realised as an integrated spring. The moving contact carrier experiences much more severe heating and melting effects as it is much thinner, which might accelerate failure in an unintended way. The thinner, moving spring contact carrier melts due to increased heat build-up. However, such failure should be carefully examined as it significantly depends on the design and dimension of the contact-carriers in the EMR. To reduce the heat build-up whilst testing in a DC setting, the experimental design can specify the static contact carrier side as anode [1]. Testing under elevated ambient temperature, will reduce arcing and erosion respectively, but might increases degradation effects like contact corrosion or the possibility of coil failure [9]. Parameters in order to accelerate EMR degradation are discussed in Table 8

APPENDIX C
CONTACT MAKING
A. WAVEFORM

An arc establishes, if the voltage across two contacts is higher than the breakdown voltage and the travel time to make contact is longer than the minimum time necessary for the discharge. This type of arc is sometimes termed *pre-strike* arc and it might be of very short duration. It can be observed, that a voltage increase relates to a decreased time to discharge, allowing for sufficient arcing already in closely-spaced, fast-closing contacts.

In Fig. 20 the first contact making is established at 0.5 ms. The voltage drops and the current increases as the contact is established among the conducting *a-spots*. However, due to the kinetic energy preserved in the contacts the moving-contact-carrier bounces back as can be seen around 0.6 ms. A molten metal bridge forms and ruptures causing a very short metallic-arc. As the contact gap is widening, the arc transfers to an ambient-gaseous-arc, which is accompanied by a voltage spike prior to settling around the minimum arc voltage of 13 V at 0.65 ms. The voltage spike is caused by the high pressure metal vapour region between the closely space contacts, initially allowing no conduction to be established within the metallic particle cloud [126]–[128]. The arc reaches its maximum length approximately at 0.7 ms

TABLE 8. Parameters to consider when testing EMR.

Variable	Description
Power	
AC	In AC application the contacts constantly change polarity. Hence the anodic and subsequent cathodic erosion lead to a comparable net erosion on both contacts.
DC	Contrary, the polarity of the contacts in DC applications does not change. Hence, typically the majority of erosion is encountered on the anode (craters). The cathode gains material (pips). Refer to Section II-B1.
Load	
Lamp	A high inrush current and variations of contact bounce accelerate contact erosion.
Inductive	In DC circuits inductive loads can cause a current lag of up to $7ms$ [53]. This leads to longer lasting arcs during *break*, while no arcing and therefore no erosion takes place during *make*, due to the current lag. Effects of bouncing might become irrelevant, refer to Section II-B2.
Resistive	Purely resistive loads have the smallest effect on contact erosion as inductive effects are mitigated, though arcing during bouncing has to be considered.
Contact Bounce	
	Contact bounce can lead to contact welding. The frequency of short unstable welds typically increases towards the EOL as the contact force and the over-travel are being reduced [124]. Notice, in DC circuits the contribution of the one-sided material loss is problematic. The frequency of the re-bounce effects the rate of erosion. High-frequent, short-gap bouncing accounts for the highest material transfer rates [1].
Sealing	
Enclosed	The contact life might be considerably longer if contacts are tested in a plastic enclosure typically found as a sealing enclosure in many EMR applications [69]. The out-gassing of the plastic leads to a contamination of the contact surfaces through deposited particles and the arc moves across the contact surface at each operation. This in turn leads to an even degradation of the entire surface. Contact life can be increased through adsorption effects from *getter-materials* used to reduce contact degradation through film-formation adsorbing harmful molecules [53].
Unsealed	The arc will more likely develop a static anode and cathode fall region, accelerating the degradation process at these spots and leading to earlier failures. Effects of contact activation and reaction of the contact material with the ambient air should be taken into account.
Arcing Suppression	
Protective Gas	Testing contacts in inert gases or nitrogen will increase the contact life and mitigate contact contamination effects.
Blowout Magnet	For DC a permanent magnetic field next to the contacts can be introduced into the EMR design to reduce effects of arcing when switching an inductive load as the arc is drawn away from the contact dispersing heat [53], [125]. Hence, such contacts are subjected to reduced rates of electrical erosion.
Switching Frequency	
	The switching frequency depends on the operate and release properties of the EMR, subject to the contact mass and velocity. In the presence of arcing, heat dissipation from the contacts should be considered, in order to not falsify the failure mode.

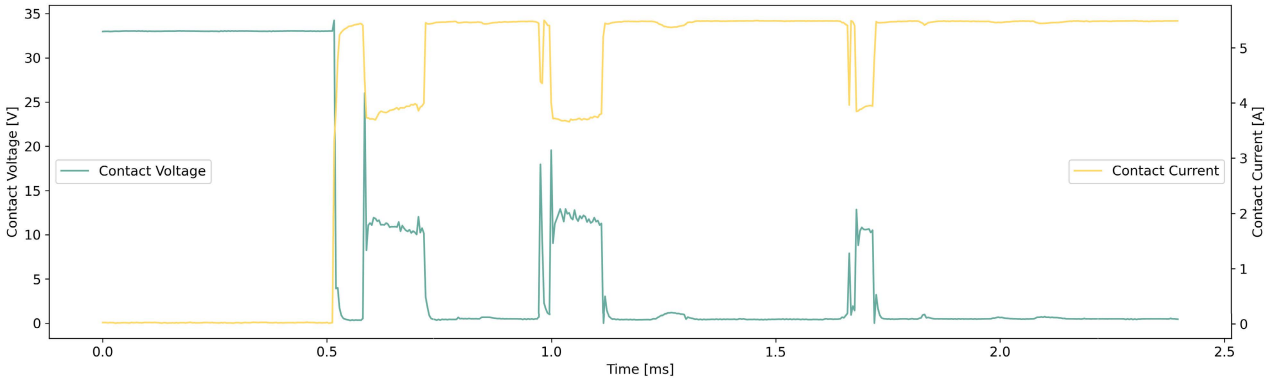

FIGURE 20. Voltage and current waveform for a making actuation; EMR ($AgSnO_2In_2O_3$)-plated copper contacts; measurements obtained during the experiment.

as the contacts start to close again. The contribution of the first arc to the degradation will be comparably higher than those of any following bouncing related arc events during one actuation if it is the predominant arcing event [1]. As the contacts touch the 2^{nd} time at 0.8 ms, the arc is extinct as the voltage drops. On this second bounce, the contacts essentially close on a molten metal surface, due to the heating of the arc. This damps the impact of the contacts and further reduces the kinetic energy. However, it is here where contact welding might occur. The duration of the continuing bounces decreases - one can observe a second and third arc, each shorter in duration than the previous one - as the preserved kinetic energy of the contacts decreases. Due to the effects of electric arcs, the decrease of kinetic energy of the contacts is accelerated compared to a decrease by purely mechanical bouncing. Lastly the contacts settle at 1.8 ms as

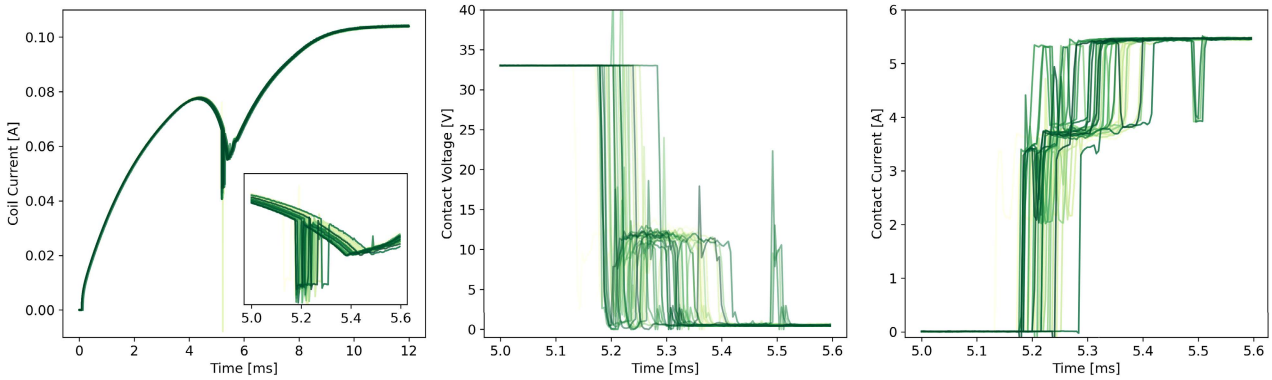

FIGURE 21. Contact making waveform from the first actuation (yellow) to EMR-EOL (green). CC (left), CV (centre), CI (right).

the contact force becomes larger than the remaining kinetic energy.

B. DETERIORATION

In Fig. 21, the changes of the raw CV and CI waveform of the making actuation throughout the EMR life are displayed. The change in time-based reference DIs during making is apparent if compared to the CC waveform. Further, the intensity and frequency of contact bouncing becomes more prominent towards the EOL.

C. FEATURES

Fig. 22 displays statistical features extracted from one sample in the selected F_S data sets. Fig. 23 depicts the trends of time-based reference DIs.

APPENDIX D
CONTACT BREAKING

A. WAVEFORM

When metallic, current carrying contacts separate, an instantaneous sequence commences. A large number of research projects have dealt with this topic, trying to empirically understand the processes involved and to determine the underlying physical phenomena [66], [129], [130]. In general EMR contacts break as follows: 1^{st}, as the contact force decreases and the contacts part, the voltage increases due to a reduction in the number of current carrying *a-spots*. Hence, the effective contact area is reduced. This process of opening is accelerated by the so called *blow-off force*, which is a result of the increasingly restricted current flow through the diminishing effective contact area [131]. This force will reduce quickly as the contacts further open and is substituted by forces stemming from the electrical arc. During the initial phase the voltage increases above the static voltage of the closed contacts; as the contact surface decreases further, the local restriction of the current flow heats up the remaining contact spots. Reaching the melting temperature at the contact spots, a bridge of molten metal will form and span between the parting contacts. Meanwhile a steady voltage increase can be observed, whereas the melting voltage is comparable with the quasi-static voltage for currents below 100 A [126]. 2^{nd}, during the stable phase, the voltage increases. This can be observed for all current-levels, in an air environment as well as in vacuum [128]. Different mechanism contribute to the material transfer as the contacts separate, some attributed to the *Thomson-Effect* [53]. However, [132] argues, the gross of material transfer is subject to electromigration. It is reasoned that electromigration will be predominant as molten metal bridges typically have small diameters. Hence, high current densities and elevated temperatures increase the rate of diffusing ions, where the temperature varies between the melting and boiling point of the metal. As the contacts further separate the 3^{rd} regime commences. The bridge becomes increasingly unstable, ultimately leads to its rupture. This phase distinguishes itself by its oscillating voltage fluctuations, spiking up to the minimum arc voltage and dropping down to the melting voltage. Though, such voltage spikes can have a stabilising effect on the bridge. Due to the increased power more metal is molten at the bridge root and sustaining the elongating bridge, whilst increasing its diameter. Vice versa, the current density is reduced, which minimises thermal stress. However, a set of interacting processes excite the molten metal bridge rupture e.g., the temperature in the bridge might reach the boiling temperature of the material, hydrodynamical-instabilities in the material, dynamic changes in surface tension as the bridge stretches as well as magnetic pinch forces depending on the carried current [126], [133]. Following the rupture of the molten metal bridge, the 4^{th} phase commences as an initial arc forms, also referred to as *bridge-column* arc or *pseudo-arc* [133]. However, is it important to emphasise that the arc will only form, once the bridge has ruptured [128]. Metal vapour, consisting out of around 5 % of the particles from the molten bridge rupture, remains in the contact gap. At this very initial stage and prior to the bridge-column arc, a non-equilibrium high pressure zone establishes, characterised by the high density metal vapour and very low conductance [124], [128]. Thereby, the voltage rapidly increase between the contacts and peaks as the

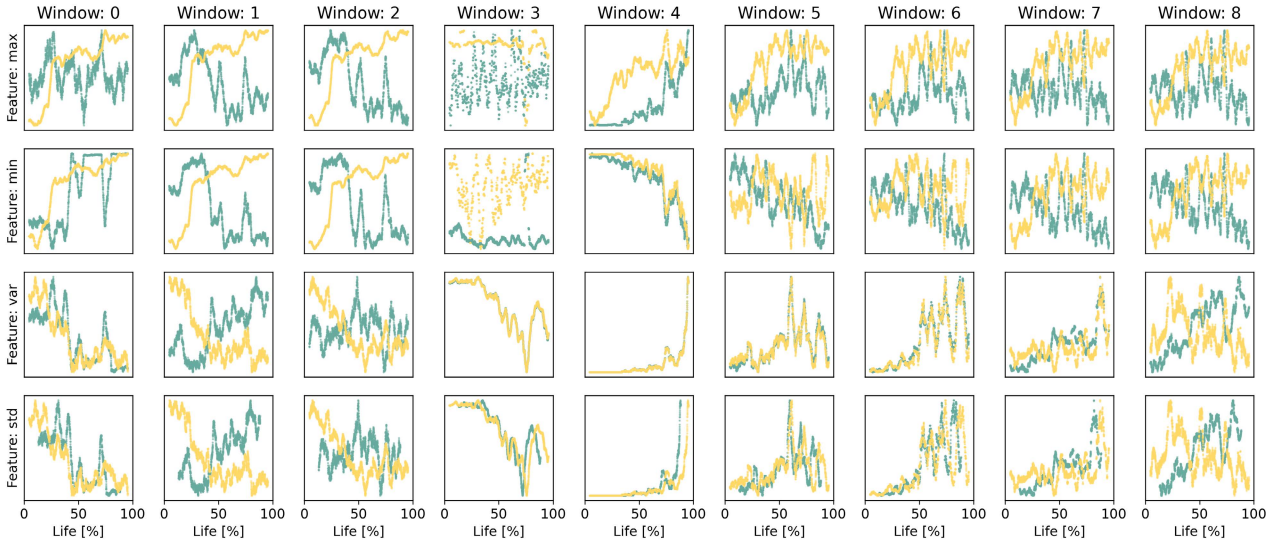

FIGURE 22. Selected statistical features of one EMR contained in F_S (from contact making).

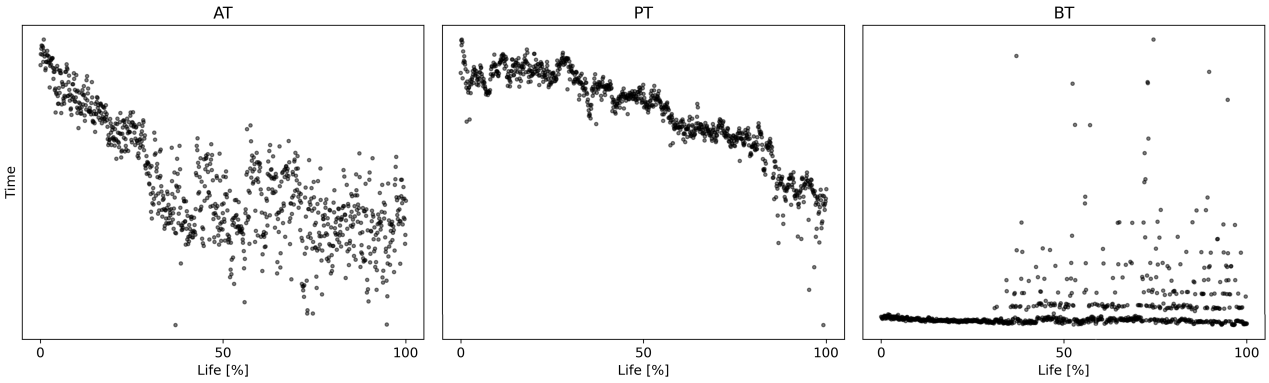

FIGURE 23. Selected time-based reference DIs of one EMR contained in F_T (from contact making). Arcing Time (AT), Pick-Up Time (PT), Bounce Time (BT).

pressure begins to fall to $2-3$ bar decaying as quickly [1]. Now, the area between the contacts acts like a capacitor with a very small capacitance [128]; remaining charges from the circuit inductance, which prevent such an instantaneous change in current, flow into this capacitor. At last, the bridge-column arc is established as the current carrying ions impact the cathode at the origin of the molten metal bridge. High erosion rates resulting in material transfer from anode to cathode can be observed during this phase as most current is carried by ions. Because the pressure continues to fall, the bridge column arc changes into a normal arc operating predominantly in the ambient gas rather than the metal vapour at a voltage around the material dependent minimum arc-voltage. Material transfer continues from anode to cathode, though the transfer rate decreases.

Following the breakdown of the molten metal bridge, detailed above, exemplary one can see the process of ambient air arc establishment, sustainment and extinguishment in the recorded breaking actuation in Fig. 24. First, the contact gap increases, the voltage spikes, then settles around 13 V across the contacts - the minimum arc voltage for copper-contacts as reported in [1]. An instantaneous current drop to 5 A follows, the initial arc establishes at 0.95 ms. Now, the metallic-arc starts transferring to an arc burning in ambient air. The arc begins to lengthen, due to the contact parting. Simultaneously the arc diameter shrinks. This causes an increase in voltage. The waveform of the current and voltage behave increasingly linear and smooth at higher current levels during contact breaking. Though, at relatively low current-levels, as in Fig. 24, a distinct sequence of voltage steps and fluctuation can be differentiated. [134] report the occurrence of those distinct steps. The initial voltage step can always be observed, though, the probability of subsequent steps decreases as the circuit voltage is increased. However, the steps observed in Fig. 24 are not as distinct despite the relatively low switching voltage. This can be attributed to the fast switching of the

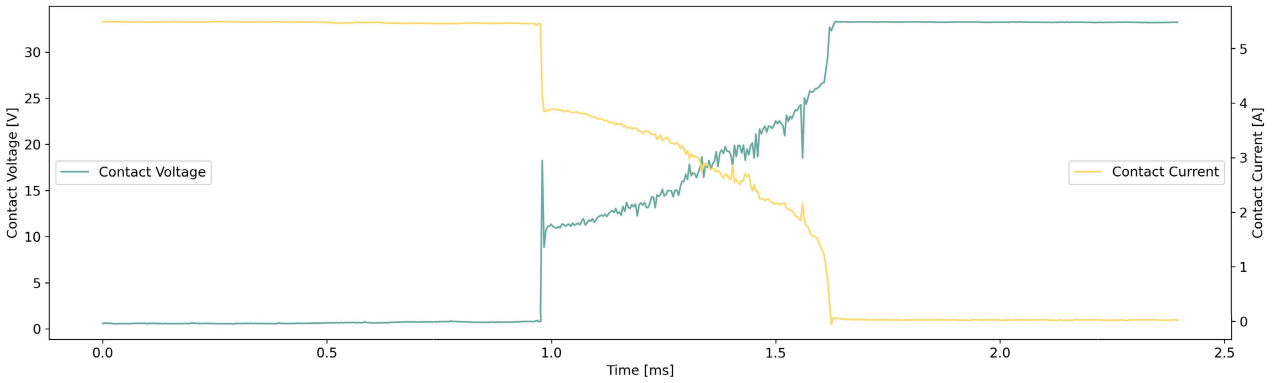

FIGURE 24. Voltage and current waveform for a breaking actuation; EMR ($AgSnO_2In_2O_3$)-plated copper contacts; measurements obtained during the experiment; refer to Section V-A.

EMR contacts (around 0.6 ms to complete the opening of the contacts). The spike of voltage and current at around 1.0 ms might be attributed to the ongoing transfer from metallic to ambient air arc [135], because the metal vapour in the contact gap is still diffused by the molecules of the ambient air and no longer able to maintain the discharge of the electric arc. However, [136] shows that such behaviour can also be observed in vacuum and therefore the explanation of this phenomenon given by [135] does not yet provide a satisfactory answer. Prior to 1.6 ms, one can observe a sharp decrease in current turning the energy balance of the arc negative i.e, the arc looses more energy than supplied through the cathode. Hence, it becomes unstable, the current drops below 1 A, and the voltage reaches 30 V. Subsequently the arc is extinct at 0.5 A which agrees with the measurements reported by [137].

B. DETERIORATION

Fig. 25 presents the changes of the breaking actuation. An increase in RT can be observed.

C. FEATURES

Fig. 26 displays selected features from the data set F_S attributed to contact breaking. As shown in Fig. 27, AT increases during contact breaking, as the longer duration of the arc increases the rate of electrical erosion on the contact surface. This accelerates the degradation process throughout the EMR life. A reason for this increase in AT is the growing surface roughness of the contacts, a decreasing contact spring force, reduction in the contact thickness leading to longer contact travel, and contamination on the contact surface lowering the required minimum arcing-voltage. Likewise, the RT exhibits an increase in duration, either indicating an increase in coil resistance and delaying the travel of the armature, or a more frequent sticking of the contacts (sometimes referred to as micro-welding) in combination with a decreasing spring force, causing a slower retraction of the contacts from each other.

APPENDIX E
CR FLUCTUATIONS IN SILVER-PLATED CONTACTS

Silver contacts - designed as pure silver, silver-alloy or silver-metal oxide contacts - are widely used as EMR contacts, either welded on the contact carrier or as contact-rivet. Beside economical factors, silver-based contacts exhibit low CR, due to low oxidation rates despite the temperature increase on the contact surface initiated through electrical arcing [138]. Additionally, the oxides formed from silver are unstable at higher temperatures. However, as pure silver has a high tendency for contact welding, typically silver-composite materials are used. Internal oxidation of these materials can reduce the weld strength, increase the material hardness, reduce contact sticking and material loss [3], [4]. However, an operating temperature increase can be observed relating to a decrease of the electric conductivity as the material's oxidisation rate and its resistance against arcing rises [139]. Manufactured using internal-oxidisation, EMR applications typically utilise these silver-metal oxides in low power applications of up to 20 A [3]. Up to 15 % oxides are found in these types of contacts [65]. Predominant failure mechanisms are due to arcing leading to contact erosion. The surface material decomposes, through evaporation, splattering or welding as the silver and the oxidised metal dissociates [140]. Contact material improvement is an active field of research e.g., [62] and [2] reporting results of contact erosion rates for silver-oxide contacts subjected to higher load currents. Toxic Silver-Cadmium-Oxide ($AgCdO$) contacts exhibit lower erosion rates than Silver-Tin-Oxide ($AgSnO_2$) contacts. This is due the comparably higher energy required for arcing on $AgSnO_2$ contacts. Hereinafter, oxidised Silver-Tin-Indium ($AgSnO_2In_2O_3$) contacts show even further reduced rates of erosion in comparison to e.g., $AgCdO$ contacts [139].

Certainly, silver-based contact material improves the performance of the contact-material. However, in terms of contact health monitoring, such contacts pose a challenge. Research has shown that EMRs equipped with silver-based contacts operating in normal, ambient air are prone to erratic

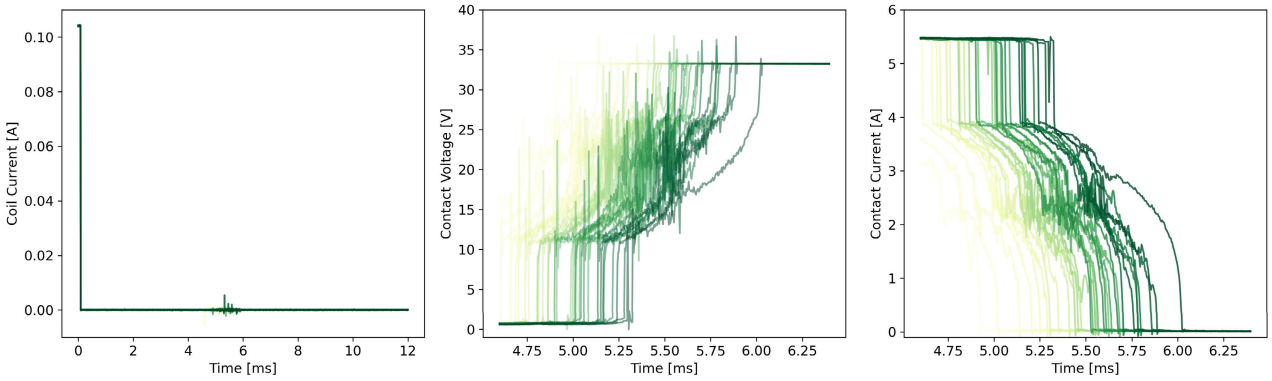

FIGURE 25. Contact breaking waveform from the first actuation (yellow) to EMR-EOL (green); CC (left), CV (centre), CI (right).

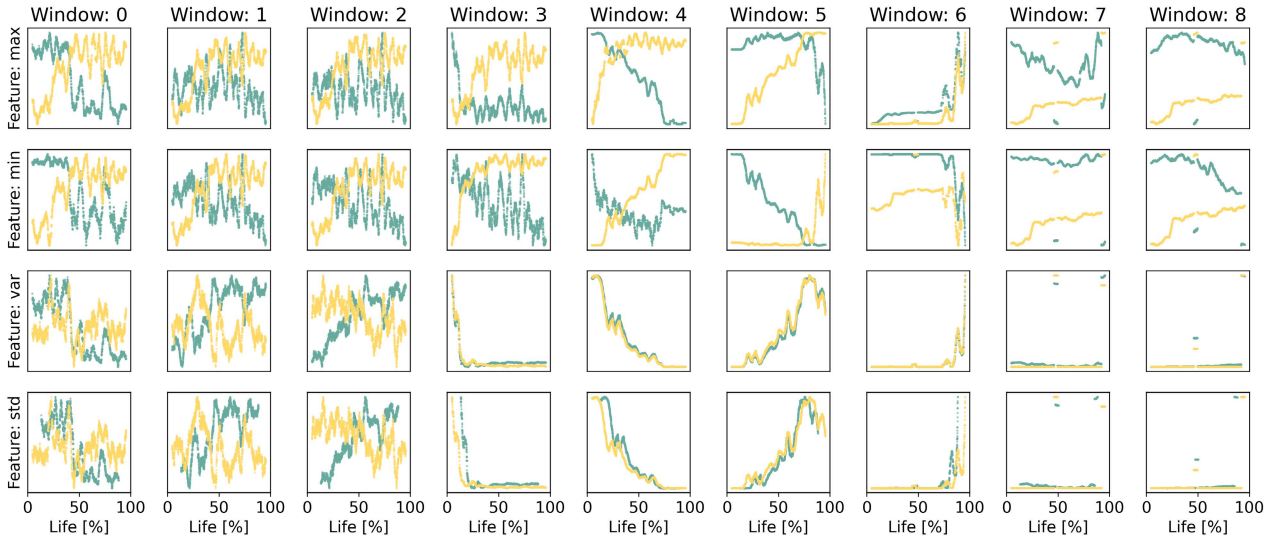

FIGURE 26. Selected statistical features of one EMR contained in F_S (from contact breaking).

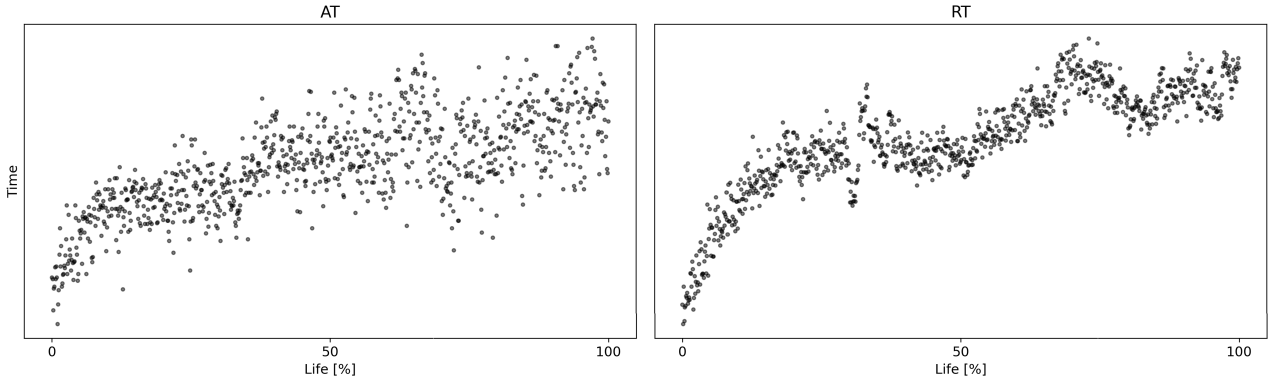

FIGURE 27. Selected time-based reference DIs of one EMR contained in F_T (from contact breaking). Arcing Time (AT), Release Time (RT).

fluctuations of CR. [1] provides some references, demonstrating that for load currents beyond 0.2 A the CR either starts fluctuating after an initially stable phase or from the start throughout the entire duration of the experiment. The rate and

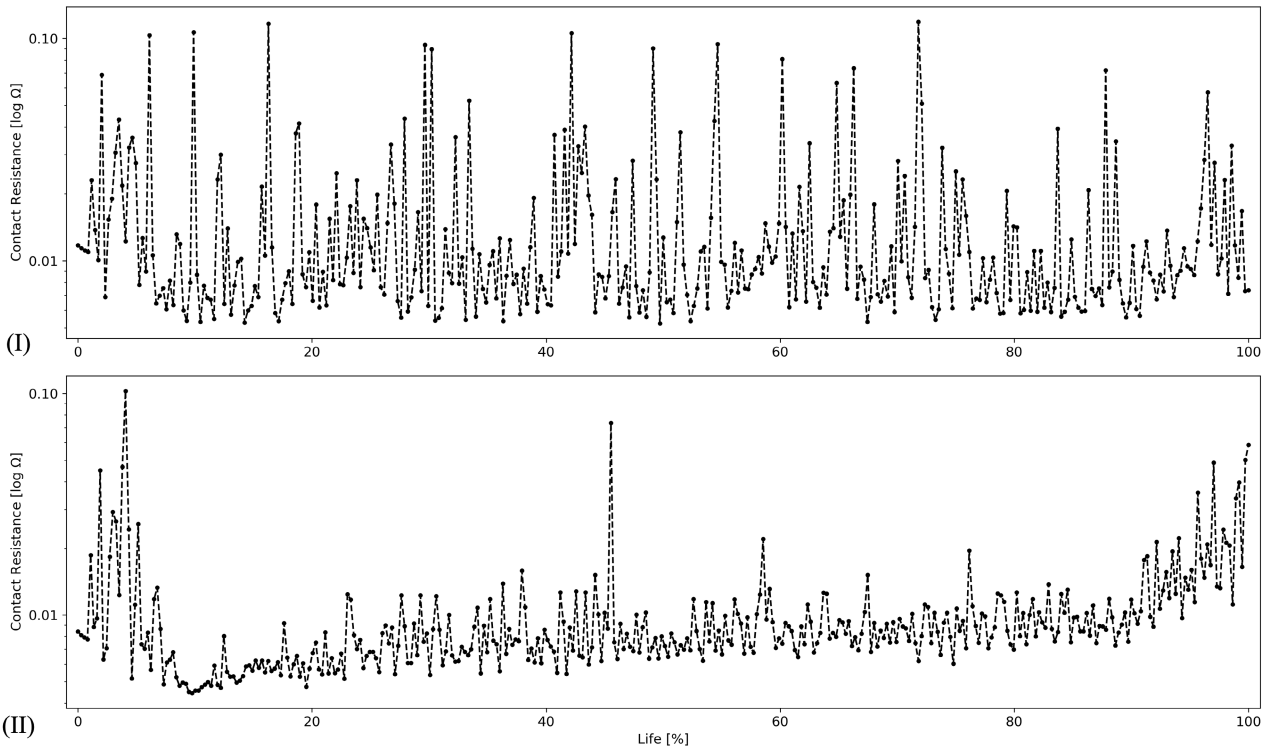

FIGURE 28. Examples of CR measurements recorded during the life cycle experiments. (I) an unsealed EMR (operated in ambient air); (II) a sealed EMR (no exposure to the ambient air).

amplitude of the fluctuations increases as the load increases. This can be linked to the growing fretting rate as well as contact erosion if arcing becomes the dominant degradation driver over the plastic deformation encountered at lower load currents. High CR values can be observed after several, long-duration gaseous-arcing events ($>$ 1 ms) [59], [141]. If arcing is only of short duration e.g., an electric arc operating only in metal vapour at very low load current, the amplitude of CR fluctuations is comparably lower. If shorter arcing changes to extended arcing, an almost instantaneous increase in CR can be observed, remaining high as long as the arc does not shorten [141]. The reduction in CR as the arcing duration shortens appears gradually. Relying on surface roughness measurements, the authors conclude that this increase and subsequent decrease of CR is attributed to changes in the contact surface. Nonuniform deposition of transferred material alters the contact morphology and the effective contact area respectively, chaining the contact spots at each making and breaking operation. However, as [59], [63] experimentally demonstrate, these CR fluctuations are dominated by non-conductive oxide film formation on the contact surface surpassing the effects of contact morphology alterations as the contact load increases. An analysis of the contact surface reveals build-up of absorbed oxygen contaminating the contact surface; these oxidised spots being preferable hit by the arc root, due to the electric field-enhancement effect [64]. Metallic- and gaseous-arcs exhibit different deposition mechanisms relevant to contact oxidisation and CR fluctuations. If the load current is high, the duration of the gaseous-arc following the metallic-arc lengthens and degradation mechanisms during the gaseous-arc phase become predominant. During the relative short metallic-arc, anode contamination films are removed due to electron sputtering as elaborated in Section II-B1, which leads to a material transfer from anode to cathode. Respectively, this contaminates the cathode surface during the metallic-arc. As [64] demonstrate, the presence of oxygen affects the metallic phase arc. The minimum arc voltage to sustain a metallic-arc is lowered in an oxygen atmosphere compared to the minimum arc voltage in a nitrogen atmosphere. The authors find this to be true even for very small concentrations of oxygen. Recall, however, that the metallic-arc is operating in a high-pressure zone within the metal-vapour matrix, hence the type of atmosphere should be insignificant for the required minimum-arc voltage. Therefore, it can be concluded that preceding oxidation of the contact surface must have taken place e.g., during storage or during a previous gaseous-arc. The direction of material transfer is reversed during the gaseous-arc phase. Unlike the metallic-arc, the gaseous-arc is exposed to higher concentrations of oxygen within the contact gap. Such arcing regimes leave visible, dark oxidation films on the anode surface, forming non-conductive contamination layers. Nonetheless, oxide films can also form around the arcs vicinity on the cathode, in a circular pattern. In case the

cathode is subjected to ion-sputtering, the cathode's surface is cleaned. A reduction in thickness of the developed oxide contact films promotes the formation of metallic clusters at the contact surface [63]. Further material accumulates on the anode, because it is transferred from the cathode to the anode during arcing. The silver-oxides are only stable at lower temperature, the majority of silver-oxides stems from silver being oxidised in the extinguishing gaseous-arc.

The CR fluctuations depend on a multitude of factors. [63] demonstrate that the contamination film thickness on the anode as well as the CR increases with increasing oxygen concentration and arc-duration. As per silver-based contacts, the gross of the CR fluctuation can be attributed to the deposition of silver-oxide films on the contact surface, increasing CR and on the other hand ion-sputtering cleaning the contacts, thus, reducing CR. The presence of even small traces of oxygen reduces the minimum required arcing-voltage extending the arcing duration whilst producing highlighted spots for electrical arcing. Slower contact velocity or switching frequency promotes higher rates of oxidation and can be linked to CR fluctuations [11], [99]. Further, CR fluctuations manifest as contact degradation which is accelerated by the reduction of conducting paths i.e., *a-spots*, due to shifting oxide contamination patches and the oxide debris deposited on the surface. Mechanical rupture of oxide films might increase or decrease CR. However, [1] annotates, that oxide film formation is only dominant when small amounts of carbons are available i.e., contact activation does not play a significant role. Otherwise, the oxide layer is replaced by silver carbonate layers. Its further worth mentioning, that fluctuations of CR can also be caused by silicon-vapours dissolved from e.g., the EMR enclosure [78].

To illustrate the challenges when relying on CR as DI (discussed in Section II-C), we consider the effect of the environment in which silver-based EMR contacts are operated in. Therefore, a comparison of CR recorded during the conducted EMR life cycle experiments for a sealed and unsealed EMR is presented. First, CR measurements for ($AgSnO_2In_2O_3$) plated EMR contacts exposed to ambient air (unsealed), operating at 6 A restive load are shown in Fig. 28-(I). Significant CR fluctuations up to 100 $m\Omega$ throughout the entire EMR life are evident, exceeding the maximum rated CR. Such *anomalies* are indistinguishable from the final rise in CR prior to the EOL and mask any underlying trend as reported in [55]. The findings align with results in [59], [63], [95], [141].

On the contrary, in Fig. 28-(II), the same contact type of ($AgSnO_2In_2O_3$) plated EMR contacts is operated in a sealed enclosure, without exposure to oxygen from the ambient air. Initially, the contacts also exhibit high CR fluctuations, due to the *burn-in* phase, where small trace amounts of residue oxygen have already been deposited on the surface. This has been reported by [142], stating that oxide deposition can occur on EMR contacts despite sealing. However, at around 10 % of the EMR the CR stabilises and increases continuously till EOL. Concluding, the operating environment in combination with the contact material and electrical arcing renders CR unsuitable as DI for silver-based EMR contacts exposed to ambient air. In the case of sealed EMR, CR holds value for maintenance purposes, though obtaining accurate CR measurements is laborious.

REFERENCES

[1] P. G. Slade, *Electrical Contacts: Principles and Application*. Boca Raton, FL, USA: CRC Press, 2017.

[2] J. Swingler and J. W. McBride, "The erosion and arc characteristics of Ag/CdO and Ag/SnO_2 contact materials under dc break conditions," *IEEE Trans. Compon., Packag., Manuf. Technol. A*, vol. 19, no. 3, pp. 404–415, Sep. 1996, doi: 10.1109/95.536842.

[3] T. Mutzel and R. Niederreuther, "The influence of switching arcs on contact resistance of Ag/SnO_2 materials," in *Proc. IEEE 61st Holm Conf. Electr. Contacts (Holm)*, Oct. 2015, pp. 171–175, doi: 10.1109/holm.2015.7355092.

[4] A. Ksiazkiewicz and J. Janiszewski, "Welding tendency for selected contact materials under different switching conditions," *Eksploatacja Niezawodnosc, Maintenance Rel.*, vol. 21, no. 2, pp. 237–245, 2019, doi: 10.17531/ein.2019.2.7.

[5] F. Yao, J. Lu, J. Zheng, and Z. Huang, "Research on the failure diagnostics parameters and the reliability prediction model of the electrical contacts," in *Proc. 52nd IEEE Holm Conf. Electr. Contacts*, Sep. 2006, pp. 69–72, doi: 10.1109/holm.2006.284067.

[6] Y. Xuerong, Y. Qiong, and Z. Guofu, "Reliability assessment for electromagnetic relay based on time parameters degradation," in *Proc. 11th Int. Conf. Electron. Packag. Technol. High Density Packag.*, Aug. 2010, pp. 1269–1272, doi: 10.1109/icept.2010.5582785.

[7] Q. Yu, M. Qi, S. Wang, and G. Zhai, "Research on life prediction based on wavelet transform and ARMA model for space relay," in *Proc. 4th IEEE Conf. Ind. Electron. Appl.*, May 2009, pp. 1275–1280, doi: 10.1109/iciea.2009.5138407.

[8] S. Sravanthi, R. Dheenadhayalan, M. P. Sakthivel, K. Devan, and K. Madhusoodanan, "A method for online diagnostics of electromagnetic relays against contact welding for safety critical applications," *IEEE Trans. Compon., Packag., Manuf. Technol.*, vol. 5, no. 12, pp. 1734–1739, Dec. 2015, doi: 10.1109/tcpmt.2015.2498624.

[9] J. Liu, M. Zhang, N. Zhao, and A. Chen, "A reliability assessment method for high speed train electromagnetic relays," *Energies*, vol. 11, no. 3, p. 652, Mar. 2018, doi: 10.3390/en11030652.

[10] F. Yao, Z. Li, W. Li, and K. Li, "Concerning contact resistance prediction based on time sequence and distribution character," in *Proc. 50th IEEE Holm Conf. Electr. Contacts 22nd Int. Conf. Electr. Contacts*, Sep. 2004, pp. 447–452, doi: 10.1109/holm.2004.1353155.

[11] A. J. Wileman and S. Perinpanayagam, "A prognostic framework for electromagnetic relay contacts," in *Proc. PHM Soc. Eur. Conf.*, vol. 2, no. 1, 2014, pp. 1–7. [Online]. Available: https://papers.phmsociety.org/index.php/phme/article/view/1531, doi: 10.36001/phme.2014.v2i1.1531.

[12] J. Guo, G. Zhang, Y. Bi, and Y. Li, "Life prediction of automotive electromagnetic relay based on wavelets neural network," *Chem. Eng. Trans.*, vol. 62, pp. 1213–1218, Dec. 2017, doi: 10.3303/CET1762203.

[13] E. Miguelañez-Martin and D. Flynn, "Embedded intelligence supporting predictive asset management in the energy sector," in *Proc. Asset Manage. Conf.*, 2015, pp. 1–7, doi: 10.1049/cp.2015.1752.

[14] V. Robu, D. Flynn, and D. Lane, "Train robots to self-certify their safe operation," *Nature*, vol. 553, no. 7688, p. 281, Jan. 2018, doi: 10.1038/d41586-018-00646-w.

[15] X. Zhao, W. Huang, A. Banks, V. Cox, D. Flynn, S. Schewe, and X. Huang, "Assessing the reliability of deep learning classifiers through robustness evaluation and operational profiles," 2021, *arXiv:2106.01258*.

[16] W. Tang, R. Dickie, D. Roman, V. Robu, and D. Flynn, "Optimisation of hybrid energy systems for maritime vessels," *J. Eng.*, vol. 2019, no. 17, pp. 4516–4521, Jun. 2019, doi: 10.1049/joe.2018.8232.

[17] K. Goebel, M. J. Daigle, A. Saxena, I. Roychoudhury, S. Sankararaman, and J. R. Celaya, *Prognostics: The Science of Making Predictions*. Scotts Valley, CA, USA: CreateSpace Independent Publishing Platform, 2017.

[18] K. Javed, R. Gouriveau, and N. Zerhouni, "State of the art and taxonomy of prognostics approaches, trends of prognostics applications and open issues towards maturity at different technology readiness levels," *Mech. Syst. Signal Process.*, vol. 94, pp. 214–236, Sep. 2017, doi: 10.1016/j.ymssp.2017.01.050.

[19] H. Meng and Y.-F. Li, "A review on prognostics and health management (PHM) methods of lithium-ion batteries," *Renew. Sustain. Energy Rev.*, vol. 116, Dec. 2019, Art. no. 109405, doi: 10.1016/j.rser.2019.109405.
[20] M. Pecht, "Prognostics and health management of electronics," in *Encyclopedia of Structural Health Monitoring*. Hoboken, NJ, USA: Wiley, 2009.
[21] L. Kirschbaum, D. Roman, G. Singh, J. Bruns, V. Robu, and D. Flynn, "AI-driven maintenance support for downhole tools and electronics operated in dynamic drilling environments," *IEEE Access*, vol. 8, pp. 78683–78701, 2020, doi: 10.1109/ACCESS.2020.2990152.
[22] M. Pecht and M. Kang, *Prognostics and Health Management of Electronics: Fundamentals, Machine Learning, and the Internet of Things*. Hoboken, NJ, USA: Wiley, 2018.
[23] D. Roman, S. Saxena, V. Robu, M. Pecht, and D. Flynn, "Machine learning pipeline for battery state-of-health estimation," *Nature Mach. Intell.*, vol. 3, no. 5, pp. 447–456, May 2021, doi: 10.1038/s42256-021-00312-3.
[24] D. Roman, S. Saxena, J. Bruns, R. Valentin, M. Pecht, and D. Flynn, "A machine learning degradation model for electrochemical capacitors operated at high temperature," *IEEE Access*, vol. 9, pp. 25544–25553, 2021, doi: 10.1109/access.2021.3057959.
[25] O. Fink, Q. Wang, M. Svensén, P. Dersin, W.-J. Lee, and M. Ducoffe, "Potential, challenges and future directions for deep learning in prognostics and health management applications," *Eng. Appl. Artif. Intell.*, vol. 92, Jun. 2020, Art. no. 103678, doi: 10.1016/j.engappai.2020.103678.
[26] Y. Zheng, Q. Liu, E. Chen, Y. Ge, and J. L. Zhao, "Time series classification using multi-channels deep convolutional neural networks," in *Proc. Int. Conf. Web-Age Inf. Manage.* Cham, Switzerland: Springer, 2014, pp. 298–310, doi: 10.1007/978-3-319-08010-9_33.
[27] J. B. Yang, M. N. Nguyen, P. P. San, X. L. Li, and S. Krishnaswamy, "Deep convolutional neural networks on multichannel time series for human activity recognition," in *Proc. 24th Int. Conf. Artif. Intell. (IJCAI)*. Palo Alto, CA, USA: AAAI Press, 2015, pp. 3995–4001. [Online]. Available: https://dl.acm.org/doi/10.5555/2832747.2832806
[28] Y. Zheng, Q. Liu, E. Chen, Y. Ge, and J. L. Zhao, "Exploiting multi-channels deep convolutional neural networks for multivariate time series classification," *Frontiers Comput. Sci.*, vol. 10, no. 1, pp. 96–112, Feb. 2016, doi: 10.1007/s11704-015-4478-2.
[29] D. Verstraete, A. Ferrada, E. L. Droguett, V. Meruane, and M. Modarres, "Deep learning enabled fault diagnosis using time-frequency image analysis of rolling element bearings," *Shock Vib.*, vol. 2017, pp. 1–17, Oct. 2017, doi: 10.1155/2017/5067651.
[30] X. Ding and Q. He, "Energy-fluctuated multiscale feature learning with deep ConvNet for intelligent spindle bearing fault diagnosis," *IEEE Trans. Instrum. Meas.*, vol. 66, no. 8, pp. 1926–1935, Mar. 2017, doi: 10.1109/TIM.2017.2674738.
[31] G. S. Babu, P. Zhao, and X.-L. Li, "Deep convolutional neural network based regression approach for estimation of remaining useful life," in *Proc. Int. Conf. Database Syst. Adv. Appl.* Cham, Switzerland: Springer, 2016, pp. 214–228, doi: 10.1007/978-3-319-32025-0_14.
[32] Y. Chen and H. Rangwala, "Attention-based multi-task learning for sensor analytics," in *Proc. IEEE Int. Conf. Big Data (Big Data)*, Dec. 2019, pp. 2187–2196, doi: 10.1109/bigdata47090.2019.9006207.
[33] Z. Khan, T. Hussain, A. Ullah, S. Rho, M. Lee, and S. Baik, "Towards efficient electricity forecasting in residential and commercial buildings: A novel hybrid CNN with a LSTM-AE based framework," *Sensors*, vol. 20, no. 5, p. 1399, Mar. 2020, doi: 10.3390/s20051399.
[34] T. Le, M. T. Vo, B. Vo, E. Hwang, S. Rho, and S. W. Baik, "Improving electric energy consumption prediction using CNN and bi-LSTM," *Appl. Sci.*, vol. 9, no. 20, p. 4237, 2019, doi: 10.3390/app9204237.
[35] S. Bai, J. Z. Kolter, and V. Koltun, "An empirical evaluation of generic convolutional and recurrent networks for sequence modeling," 2018, *arXiv:1803.01271*.
[36] C. Pelletier, G. I. Webb, and F. Petitjean, "Temporal convolutional neural network for the classification of satellite image time series," *Remote Sens.*, vol. 11, no. 5, p. 523, 2019, doi: 10.3390/rs11050523.
[37] M. Nan, M. Trăscău, A. M. Florea, and C. C. Iacob, "Comparison between recurrent networks and temporal convolutional networks approaches for skeleton-based action recognition," *Sensors*, vol. 21, no. 6, p. 2051, Mar. 2021, doi: 10.3390/s21062051.
[38] J. Wenqiang, C. Jian, and C. Yi, "Remaining useful life prediction for mechanical equipment based on temporal convolutional network," in *Proc. 14th IEEE Int. Conf. Electron. Meas. Instrum. (ICEMI)*, Nov. 2019, pp. 1192–1199, doi: 10.1109/icemi46757.2019.9101706.
[39] Y. Song, S. Gao, Y. Li, L. Jia, Q. Li, and F. Pang, "Distributed attention-based temporal convolutional network for remaining useful life prediction," *IEEE Internet Things J.*, vol. 8, no. 12, pp. 9594–9602, Jun. 2021, doi: 10.1109/jiot.2020.3004452.
[40] J. Chen, D. Chen, and G. Liu, "Using temporal convolution network for remaining useful lifetime prediction," *Eng. Rep.*, vol. 3, no. 3, Mar. 2021, Art. no. e12305, doi: 10.1002/eng2.12305.
[41] A. Saxena and K. Goebel, "Turbofan engine degradation simulation data set," in *Proc. NASA Ames Prognostics Data Repository*, 2008, pp. 1551–3203.
[42] P. Nectoux, R. Gouriveau, K. Medjaher, E. Ramasso, B. Chebel-Morello, N. Zerhouni, and C. Varnier, "PRONOSTIA: An experimental platform for bearings accelerated degradation tests," in *Proc. IEEE Int. Conf. Prognostics Health Manage. (PHM)*, Jun. 2012, pp. 1–8.
[43] C. Liu, L. Zhang, and C. Wu, "Direct remaining useful life prediction for rolling bearing using temporal convolutional networks," in *Proc. IEEE Symp. Ser. Comput. Intell. (SSCI)*, Dec. 2019, pp. 2965–2971, doi: 10.1109/ssci44817.2019.9003163.
[44] W. Yang, Q. Yao, K. Ye, and C.-Z. Xu, "Empirical mode decomposition and temporal convolutional networks for remaining useful life estimation," *Int. J. Parallel Program.*, vol. 48, no. 1, pp. 61–79, Feb. 2020, doi: 10.1007/s10766-019-00650-1.
[45] D. Zhou, Z. Li, J. Zhu, H. Zhang, and L. Hou, "State of health monitoring and remaining useful life prediction of lithium-ion batteries based on temporal convolutional network," *IEEE Access*, vol. 8, pp. 53307–53320, 2020, doi: 10.1109/access.2020.2981261.
[46] B. Saha, K. Goebel, S. Poll, and J. Christophersen, "Prognostics methods for battery health monitoring using a Bayesian framework," *IEEE Trans. Instrum. Meas.*, vol. 58, no. 2, pp. 291–296, Feb. 2009, doi: 10.1109/TIM.2008.2005965.
[47] H. Wang, M. Peng, R. Xu, A. Ayodeji, and H. Xia, "Remaining useful life prediction based on improved temporal convolutional network for nuclear power plant valves," *Frontiers Energy Res.*, vol. 8, p. 296, Nov. 2020, doi: 10.3389/fenrg.2020.584463.
[48] B. Lakshminarayanan, A. Pritzel, and C. Blundell, "Simple and scalable predictive uncertainty estimation using deep ensembles," 2016, *arXiv:1612.01474*.
[49] Y. Gal and Z. Ghahramani, "Dropout as a Bayesian approximation: Representing model uncertainty in deep learning," in *Proc. Int. Conf. Mach. Learn.*, 2016, pp. 1050–1059. [Online]. Available: https://proceedings.mlr.press/v48/gal16.html
[50] H.-P. Nguyen, J. Liu, and E. Zio, "A long-term prediction approach based on long short-term memory neural networks with automatic parameter optimization by tree-structured Parzen estimator and applied to time-series data of NPP steam generators," *Appl. Soft Comput.*, vol. 89, Apr. 2020, Art. no. 106116, doi: 10.1016/j.asoc.2020.106116.
[51] M. Wei, H. Gu, M. Ye, Q. Wang, X. Xu, and C. Wu, "Remaining useful life prediction of lithium-ion batteries based on Monte Carlo dropout and gated recurrent unit," *Energy Rep.*, vol. 7, pp. 2862–2871, Nov. 2021, doi: 10.1016/j.egyr.2021.05.019.
[52] L. Kirschbaum, D. Roman, V. Robu, and D. Flynn, "Deep learning pipeline for state-of-health classification of electromagnetic relays," in *Proc. IEEE 30th Int. Symp. Ind. Electron. (ISIE)*, Jun. 2021, pp. 1–7, doi: 10.1109/isie45552.2021.9576278.
[53] H. Sauer, *Modern Relay Technology*. Heidelberg, Germany: Huethig, 1986.
[54] L. Kirschbaum, F. Dinmohammadi, D. Flynn, V. Robu, and M. Pecht, "Failure analysis informing embedded health monitoring of electromagnetic relays," in *Proc. 3rd Int. Conf. Syst. Rel. Saf. (ICSRS)*, Nov. 2018, pp. 261–267, doi: 10.1109/icsrs.2018.8688839.
[55] A. J. Wileman and S. Perinpanayagam, "Integrated vehicle health management: An approach to dealing with lifetime prediction considerations on relays," *Microelectron. Rel.*, vol. 55, nos. 9–10, pp. 2165–2171, 2015, doi: 10.1016/j.microrel.2015.06.013.
[56] Y. Sun, Y. Cao, Y. Zhang, and C. Xu, "A novel life prediction method for railway safety relays using degradation parameters," *IEEE Intell. Transp. Syst. Mag.*, vol. 10, no. 3, pp. 48–56, Mar. 2018, doi: 10.1109/MITS.2018.2842048.
[57] *Electromechanical Elementary Relays—Part 1: General and Safety Requirements*, Int. Electrotech. Commission, Geneva, Switzerland, 2015.
[58] Y. Xuerong, M. Yue, M. Hang, and Z. Guofu, "Degradation failure model of electromagnetic relay," in *Proc. 26th Int. Conf. Electr. Contacts (ICEC)*, 2012, pp. 116–123, doi: 10.1049/cp.2012.0633.

[59] Z.-K. Chen, H. Mizukoshi, and K. Sawa, "Contact resistance characteristics of Ag material in breaking low-load DC arcs," *IEEE Trans. Compon., Packag., Manuf. Technol. A*, vol. 17, no. 1, pp. 113–120, Mar. 1994, doi: 10.1109/95.296376.

[60] X. Ye, R. Fu, Y. Wu, Y. Lin, and G. Zhai, "Simulation and diagnosis of degradation failure on electromagnetic relay," in *Proc. Prognostics Syst. Health Manage. Conf. (PHM-Harbin)*, Jul. 2017, pp. 1–9, doi: 10.1109/phm.2017.8079301.

[61] R. Holm, *Electric Contacts: Theory and Application*. Cham, Switzerland: Springer, 2013.

[62] J. Swingler and A. Sumption, "Arc erosion of $AgSnO_2$ electrical contacts at different stages of a break operation," *Rare Met.*, vol. 29, no. 3, pp. 248–254, Jun. 2010, doi: 10.1007/s12598-010-0043-1.

[63] Z.-K. Chen and K. Sawa, "Effect of oxide films and arc duration characteristics on Ag contact resistance behavior," *IEEE Trans. Compon., Packag., Manuf. Technol. A*, vol. 18, no. 2, pp. 409–416, Jun. 1995, doi: 10.1109/95.390325.

[64] D. Grogg and C. Schrank, "Impact of the gas environment on the electric arc," in *Proc. IEEE 62nd Holm Conf. Electr. Contacts (Holm)*, Oct. 2016, pp. 125–128, doi: 10.1109/holm.2016.7780019.

[65] L. Yi and N. Lu, "Evaluation and comparison of the arc erosion characteristic of $Ag/SnO_2/In2O_3$ contact materials used for an automotive relay," in *Proc. IEEE Holm Conf. Electr. Contacts*, Oct. 2018, pp. 387–393, doi: 10.1109/holm.2018.8611673.

[66] P. Slade, "An investigation of current interruption in low-voltage circuits," *IEEE Trans. Parts, Mater., Packag.*, vol. PMP-5, no. 1, pp. 56–61, Mar. 1969, doi: 10.1109/TPMP.1969.1136052.

[67] W. F. Rieder, "Low current arc modes of short length and time: A review," *IEEE Trans. Compon. Packag. Technol.*, vol. 23, no. 2, pp. 286–292, Jun. 2000, doi: 10.1109/6144.846766.

[68] Z.-K. Chen and K. Sawa, "Particle sputtering and deposition mechanism for material transfer in breaking arcs," *J. Appl. Phys.*, vol. 76, no. 6, pp. 3326–3331, Sep. 1994, doi: 10.1063/1.358501.

[69] G. Witter and L. Polevoy, "Contact erosion and material transfer for contacts in automotive relays," in *Proc. 42nd IEEE Holm Conf. Electr. Contacts, Joint 18th Int. Conf. Electr. Contacts*, Sep. 1996, pp. 223–228, doi: 10.1109/HOLM.1996.557201.

[70] Z. K. Chen and G. Witter, "A comparison of contact erosion for opening velocity variations for 13 volt circuits," in *Proc. 52nd IEEE Holm Conf. Electr. Contacts*, Sep. 2006, pp. 15–20, doi: 10.1109/holm.2006.284058.

[71] W. F. Rieder and A. R. Neuhaus, "Contact welding influenced by anode arc and cathode arc, respectively," in *Proc. 50th IEEE Holm Conf. Electr. Contacts 22nd Int. Conf. Electr. Contacts Electr. Contacts*, Sep. 2004, pp. 378–381, doi: 10.1109/holm.2004.1353144.

[72] L. Zhao, Z. Li, H. Zhang, and M. Hasegawa, "Random occurrence of contact welding in electrical endurance tests," *IEICE Trans. Electron.*, vol. E94-C, no. 9, pp. 1362–1368, 2011, doi: 10.1587/transele.e94.c.1362.

[73] H. Jiang and L. Zhenbiao, "A review on welding in make and break operation of electrical contacts," in *Proc. 3rd Int. Conf. Electr. Power Equip., Switching Technol. (ICEPE-ST)*, Oct. 2015, pp. 1–5, doi: 10.1109/icepe-st.2015.7368324.

[74] X. Yang, J. Huang, Z. Li, J. Liu, Q. Wang, and M. Hasegawa, "The preceding voltage pulse and separation welding mechanism of electrical contacts," *IEEE Trans. Compon., Packag., Manuf. Technol.*, vol. 6, no. 6, pp. 846–853, Jun. 2016, doi: 10.1109/TCPMT.2016.2552202.

[75] W. Ren, Y. He, J. Jin, and S. Man, "Investigations of the contact bounce behaviors and relative dynamic welding phenomena for electromechanical relay," *Rev. Sci. Instrum.*, vol. 8, no. 6, Jun. 2016, Art. no. 065111, doi: 10.1063/1.4953838.

[76] T. Tamai, K. Miyagawa, and M. Furukawa, "Effect of switching rate on contact failure from contact resistance of micro relay under environment containing silicone vapor," in *Proc. 43rd IEEE Holm Conf. Electr. Contacts*, Oct. 1997, pp. 333–339, doi: 10.1109/HOLM.1997.638059.

[77] N. Kitchen and C. Russell, "Silicone oils on electrical contacts-effects, sources, and countermeasures," *IEEE Trans. Parts, Hybrids, Packag.*, vol. PHP-12, no. 1, pp. 24–28, Mar. 1976, doi: 10.1109/TPHP.1976.1135104.

[78] M. Hasegawa, N. Kobayashi, and Y. Kohno, "Contact resistance characteristics of relays operated in silicone-vapor-containing and non-silicone atmospheres with different electrical load conditions," in *Proc. IEEE 57th Holm Conf. Electr. Contacts (Holm)*, Sep. 2011, pp. 1–7, doi: 10.1109/holm.2011.6034787.

[79] J.-G. Zhang and X.-M. Wen, "The effect of dust contamination on electric contacts," *IEEE Trans. Compon., Hybrids, Manuf. Technol.*, vol. CHMT-9, no. 1, pp. 53–58, Mar. 1986, doi: 10.1109/TCHMT.1986.1136620.

[80] P. L. Hurricks, "The mechanism of fretting—A review," *Wear*, vol. 15, no. 6, pp. 389–409, Jun. 1970, doi: 10.1016/0043-1648(70)90235-8.

[81] A. Siddaiah, A. K. Kasar, V. Khosla, and P. L. Menezes, "*In-situ* fretting wear analysis of electrical connectors for real system applications," *J. Manuf. Mater. Process.*, vol. 3, no. 2, p. 47, Jun. 2019, doi: 10.3390/jmmp3020047.

[82] R. D. Malucci, "Impact of fretting parameters on contact degradation," in *Proc. 42nd IEEE Holm Conf. Electr. Contacts, Joint 18th Int. Conf. Electr. Contacts*, Sep. 1996, pp. 395–403, doi: 10.1109/HOLM.1996.557220.

[83] W. F. Rieder and T. W. Strof, "Relay life tests with contact resistance measurement after each operation," *IEEE Trans. Compon., Hybrids, Manuf. Technol.*, vol. 14, no. 1, pp. 109–112, Mar. 1991, doi: 10.1109/33.76518.

[84] X. Zhou, L. Zou, and R. J. Briggs, "Prognostic and diagnostic technology for DC actuated contactors and motor starters," *IEICE Trans. Electron.*, vol. 92, no. 8, pp. 1045–1051, 2009, doi: 10.1587/transele.E92.C.1045.

[85] W. Li, K. Li, L. Sun, S. Zhao, and L. Ji, "The test data verifying & prediction model of electrical contact," in *Proc. 50th IEEE Holm Conf. Electr. Contacts 22nd Int. Conf. Electr. Contacts Electr. Contacts*, Sep. 2004, pp. 429–436, doi: 10.1109/HOLM.2004.1353152.

[86] H. Liang, Q. Zhang, and G. Zhai, "Research and application of testing and analyzing system for sealed relay's time parameters," in *Proc. 50th IEEE Holm Conf. Electr. Contacts 22nd Int. Conf. Electr. Contacts Electr. Contacts*, Sep. 2004, pp. 199–205, doi: 10.1109/holm.2004.1353118.

[87] Z. Wang, S. Shang, X. Huang, G. Zhai, and W. Chen, "Research on degradation modeling of pick-up time for aerospace electromagnetic relay in long-term stockpile," in *Proc. IEEE 61st Holm Conf. Electr. Contacts (Holm)*, Oct. 2015, pp. 182–186, doi: 10.1109/holm.2015.7355094.

[88] Y. Fang, L. Zhigang, W. Yachao, and Y. Cuiping, "Research on uncertainty of bounce time for electromagnetic relay and its application in operating reliability estimation," in *Proc. 26th Int. Conf. Electr. Contacts (ICEC)*, 2012, pp. 200–204, doi: 10.1049/cp.2012.0648.

[89] X. Pang, Z. Li, M.-L. Tseng, K. Liu, K. Tan, and H. Li, "Electric vehicle relay lifetime prediction model using the improving fireworks algorithm–grey neural network model," *Appl. Sci.*, vol. 10, no. 6, p. 1940, Mar. 2020, doi: 10.3390/app10061940.

[90] Y. Sun, Y. Zhang, C. Xu, and Y. Cao, "Failure mechanisms discrimination and life prediction of safety relay," *J. Traffic Transp. Eng.*, vol. 18, pp. 138–147, Mar. 2018.

[91] C. Xinglei, Z. Xue, C. Mo, L. Fubiao, and Z. Zhefeng, "Electrical lifespan prediction of high-voltage direct-current relay based on arc charge accumulation," in *Proc. IEEE 62nd Holm Conf. Electr. Contacts (Holm)*, Oct. 2016, pp. 167–172, doi: 10.1109/holm.2016.7780027.

[92] Y. Zhao, E. Zio, and G. Fu, "Remaining storage life prediction for an electromagnetic relay by a particle filtering-based method," *Microelectron. Rel.*, vol. 79, pp. 221–230, Dec. 2017, doi: 10.1016/j.microrel.2017.03.026.

[93] A. Najam, P. Pieterse, and D. Uhrlandt, "Electrical modelling of switching arcs in a low voltage relay at low currents," *Energies*, vol. 13, no. 23, p. 6377, Dec. 2020, doi: 10.3390/en13236377.

[94] G.-F. Yu, Y.-J. Chiu, X. Zheng, Z.-L. Yuan, and Z.-X. Wang, "Contact pressure of high-voltage dc power relay change and life prediction and structure optimization," *Adv. Mech. Eng.*, vol. 13, no. 2, 2021, Art. no. 1687814021991666, doi: 10.1177/1687814021991666.

[95] K. Li, F. Yao, J. Lu, and Z. Li, "Test and analysis of reliability for electromagnetic relay," in *Proc. 46th IEEE Holm Conf. Electr. Contacts*, Sep. 2000, pp. 79–82, doi: 10.1109/HOLM.2000.889915.

[96] J. X. Wan, K. Xue, Y. Chen, and M. S. Tong, "An acquisition and processing method for the key parameters of electromagnetic relays," in *Proc. Prog. Electromagn. Res. Symp. Fall (PIERS-FALL)*, 2017, pp. 1096–1100, doi: 10.1109/piers-fall.2017.8293297.

[97] L. Li, Y. Han, W. Chen, C. Lv, and D. Sun, "An improved wavelet packet-chaos model for life prediction of space relays based on Volterra series," *PLoS ONE*, vol. 11, no. 6, Jun. 2016, Art. no. e0158435, doi: 10.1371/journal.pone.0158435.

[98] Z. Li, B. Liu, M. Yuan, F. Zhang, and J. Guo, "Characterization of initial parameter information for lifetime prediction of electronic devices," *PLoS ONE*, vol. 11, no. 12, Dec. 2016, Art. no. e0167429, doi: 10.1371/journal.pone.0167429.

[99] X. Cui, X. Zhou, G. Zhai, Z. Fang, and F. Liu, "Electrical lifespan prediction of HVDC relay based on the accumulated arc erosion mass," *IEEE Trans. Compon., Packag., Manuf. Technol.*, vol. 8, no. 3, pp. 356–363, Mar. 2018, doi: 10.1109/tcpmt.2017.2768222.
[100] Y. Sun, Y. Cao, M. Zhou, T. Wen, P. Li, and C. Roberts, "A hybrid method for life prediction of railway relays based on multi-layer decomposition and RBFNN," *IEEE Access*, vol. 7, pp. 44761–44770, 2019, doi: 10.1109/ACCESS.2019.2906895.
[101] S. Sravanthi, R. Dheenadhayalan, G. Vinod, K. Madhusoodanan, and K. Devan, "Reliability model of a relay output card with diagnostic circuitry for safety instrumented system," in *Proc. Int. Conf. Syst. Rel. Sci. (ICSRS)*, Nov. 2016, pp. 130–136, doi: 10.1109/icsrs.2016.7815851.
[102] P. Wadhawan, M. Kumar, A. Mayya, and P. P. Marathe, "Comparison and failure mode analysis of current signature based relay health monitoring schemes," in *Proc. 6th Int. Conf. Rel., Infocom Technol. Optim., Trends Future Directions (ICRITO)*, Sep. 2017, pp. 155–161, doi: 10.1109/icrito.2017.8342417.
[103] Z. Wang, G. Zhai, W. Ren, X. Huang, and Q. Yu, "Research on accelerated storage degradation testing for aerospace electromagnetic relay," in *Proc. IEEE 58th Holm Conf. Electr. Contacts (Holm)*, Sep. 2012, pp. 1–8, doi: 10.1109/holm.2012.6336597.
[104] Z.-B. Wang, G.-F. Zhai, X.-Y. Huang, and D.-X. Yi, "Combination forecasting method for storage reliability parameters of aerospace relays based on grey-artificial neural networks," *Int. J. Innov. Comput., Inf. Control*, vol. 9, no. 9, pp. 3807–3816, 2013.
[105] Z. Wang, S. Shang, G. Zhai, and W. Ren, "Research on storage degradation testing and life prediction based on ARMA and wavelet transform model for aerospace electromagnetic relay," in *Proc. IEEE 60th Holm Conf. Electr. Contacts (Holm)*, Oct. 2014, pp. 1–8, doi: 10.1109/holm.2014.7031021.
[106] Z. Wang, S. Fu, S. Shang, and W. Chen, "New forecasting method of closing time for aerospace relay in storage accelerated degradation testing," in *Proc. 11th Int. Conf. Rel., Maintainability Saf. (ICRMS)*, Oct. 2016, pp. 1–5, doi: 10.1109/icrms.2016.8050118.
[107] Z. Wang, Z. Huang, J. Wang, S. Shang, and G. Zhai, "The failure mechanism of electromagnetic relay in accelerated storage degradation testing," in *Proc. IEEE Holm Conf. Electr. Contacts*, Sep. 2017, pp. 164–168, doi: 10.1109/holm.2017.8088080.
[108] Z. Wang, S. Shang, J. Wang, Z. Huang, and F. Sai, "Accelerated storage degradation testing and failure mechanisms of aerospace electromagnetic relay," *Eksploatacja i Niezawodność*, vol. 19, no. 4, pp. 530–541, Sep. 2017, doi: 10.17531/ein.2017.4.6.
[109] W. Guo, G. Fu, B. Wan, M. Jiang, and Y. Li, "Storage PoF model of electromagnetic relays based on electrical contact theory," *Microelectron. Rel.*, vols. 100–101, Sep. 2019, Art. no. 113381, doi: 10.1016/j.microrel.2019.06.073.
[110] B. Sun, X. Jiang, K.-C. Yung, J. Fan, and M. G. Pecht, "A review of prognostic techniques for high-power white LEDs," *IEEE Trans. Power Electron.*, vol. 32, no. 8, pp. 6338–6362, Aug. 2017, doi: 10.1109/TPEL.2016.2618422.
[111] A. van den Oord, S. Dieleman, H. Zen, K. Simonyan, O. Vinyals, A. Graves, N. Kalchbrenner, A. Senior, and K. Kavukcuoglu, "WaveNet: A generative model for raw audio," 2016, *arXiv:1609.03499*.
[112] K. He, X. Zhang, S. Ren, and J. Sun, "Deep residual learning for image recognition," in *Proc. IEEE Conf. Comput. Vis. Pattern Recognit. (CVPR)*, Jun. 2016, pp. 770–778, doi: 10.1109/cvpr.2016.90.
[113] M. Pecht, "IEEE standard framework for prognostics and health management of electronic systems," IEEE Standards Assoc., Piscataway, NJ, USA, Tech. Rep. 1856-2017, 2017, doi: 10.1109/IEEESTD.2017.8227036.
[114] S. L. Smith, P.-J. Kindermans, C. Ying, and Q. V. Le, "Don't decay the learning rate, increase the batch size," 2017, *arXiv:1711.00489*.
[115] A. Brando, D. Torres, J. A. Rodriguez-Serrano, and J. Vitria, "Building uncertainty models on top of black-box predictive Apis," *IEEE Access*, vol. 8, pp. 121344–121356, 2020, doi: 10.1109/access.2020.3006711.
[116] R. Seoh, "Qualitative analysis of Monte Carlo dropout," 2020, *arXiv:2007.01720*.
[117] A. Saxena, J. Celaya, B. Saha, S. Saha, and K. Goebel, "Metrics for offline evaluation of prognostic performance," *Int. J. Prognostics Health Manage.*, vol. 1, no. 1, pp. 4–23, 2010, doi: 10.36001/ijphm.2010.v1i1.1336.
[118] Y. Lei, N. Li, L. Guo, N. Li, T. Yan, and J. Lin, "Machinery health prognostics: A systematic review from data acquisition to RUL prediction," *Mech. Syst. Signal Process.*, vol. 104, pp. 799–834, May 2018, doi: 10.1016/j.ymssp.2017.11.016.
[119] V. Kuleshov, N. Fenner, and S. Ermon, "Accurate uncertainties for deep learning using calibrated regression," in *Proc. Int. Conf. Mach. Learn.*, 2018, pp. 2796–2804.
[120] Z. K. Chen and G. J. Witter, "A study of dynamic welding of electrical contacts with emphasis on the effects of oxide content for silver tin indium oxide contacts," in *Proc. 56th IEEE Holm Conf. Electr. Contacts*, Oct. 2010, pp. 1–6, doi: 10.1109/holm.2010.5619552.
[121] T. Mutzel, M. Bender, and R. Niederreuther, "The effect of material composition on dynamic welding of electrical contacts," in *Proc. IEEE 59th Holm Conf. Electr. Contacts (Holm)*, Sep. 2013, pp. 1–7, doi: 10.1109/holm.2013.6651432.
[122] S. Zheng, K. Ristovski, A. Farahat, and C. Gupta, "Long short-term memory network for remaining useful life estimation," in *Proc. IEEE Int. Conf. Prognostics Health Manage. (ICPHM)*, Jun. 2017, pp. 88–95, doi: 10.1109/icphm.2017.7998311.
[123] *Aircraft—Electromagnetic Relays and Contactors*, Int. Org. Standardization, Geneva, Switzerland, 1996.
[124] Z.-K. Chen and K. Sawa, "Effect of arc behavior on material transfer: A review," in *Proc. 42nd IEEE Holm Conf. Electr. Contacts, Joint 18th Int. Conf. Electr. Contacts*, Sep. 1996, pp. 238–251, doi: 10.1109/HOLM.1996.557203.
[125] W. Godsey, "Arc suppression for relay contacts in DC service," *IRE Trans. Compon. Parts*, vol. 4, no. 2, pp. 36–42, 1957, doi: 10.1109/TCP.1957.1135909.
[126] P. Koren, M. Nahemow, and P. Slade, "The molten metal bridge stage of opening electrical contacts," *IEEE Trans. Parts, Hybrids, Packag.*, vol. PHP-11, no. 1, pp. 4–10, Mar. 1975, doi: 10.1109/TPHP.1975.1135030.
[127] P. G. Slade, "The transition from the molten bridge to the metallic phase bridge column arc between electrical contacts opening in vacuum," in *Proc. 23rd Int. Symp. Discharges Electr. Insul. Vac.*, Sep. 2008, pp. 198–201, doi: 10.1109/deiv.2008.4676753.
[128] P. G. Slade, "Opening electrical contacts: The transition from the molten metal bridge to the electric arc," *IEICE Trans. Electron.*, vol. E93.C, no. 9, pp. 1380–1386, 2010.
[129] C. H. Leung and A. Lee, "Contact erosion in automotive DC relays," *IEEE Trans. Compon., Hybrids, Manuf. Technol.*, vol. 14, no. 1, pp. 101–108, Mar. 1991, doi: 10.1109/HOLM.1990.113001.
[130] J. Swingler, A. Sumption, and J. W. McBride, "The evolution of contact erosion during an opening operation at 42 V," in *Proc. 41st IEEE Holm Conf. Electr. Contacts*, Sep. 2005, pp. 346–351, doi: 10.1109/holm.2005.1518268.
[131] P. G. Slade and E. D. Taylor, "The repulsion or blow-off force between closed contacts carrying current," in *Proc. IEEE 62nd Holm Conf. Electr. Contacts (Holm)*, Oct. 2016, pp. 159–162, doi: 10.1109/holm.2016.7780025.
[132] R. S. Timsit, "Electromigration in a liquid bridge before contact break," in *Proc. 56th IEEE Holm Conf. Electr. Contacts*, Oct. 2010, pp. 1–6, doi: 10.1109/holm.2010.5619474.
[133] A. A. Logachev, P. A. Tenitskiy, and A. V. Vykhodtsev, "Analysis of voltage oscillograms at disconnecting contacts," in *Proc. Int. Symp. Discharges Electr. Insul. Vac. (ISDEIV)*, Sep. 2014, pp. 225–228, doi: 10.1109/deiv.2014.6961660.
[134] S. M. Abu Sharkh and J. W. McBride, "Voltage steps in atmospheric low current arcs between opening silver metal oxide contacts," in *Proc. 43rd IEEE Holm Conf. Electr. Contacts*, Oct. 1997, pp. 233–237, doi: 10.1109/HOLM.1997.638047.
[135] P. J. Boddy and T. Utsumi, "Fluctuation of arc potential caused by metal-vapor diffusion in arcs in air," *J. Appl. Phys.*, vol. 42, no. 9, pp. 3369–3373, Aug. 1971, doi: 10.1063/1.1660739.
[136] N. Vogel, "Burning voltage in atmospheric and vacuum short arcs of vanishing length," *Contributions to Plasma Phys.*, vol. 29, no. 1, pp. 11–24, 1989, doi: 10.1002/ctpp.2150290104.
[137] M. Hasegawa, Y. Tamaki, and Y. Kamada, "An experimental study on minimum arc current of relay contacts and possible re-interpretation of the meaning thereof," in *Proc. 52nd IEEE Holm Conf. Electr. Contacts*, Sep. 2006, pp. 153–158, doi: 10.1109/holm.2006.284080.
[138] L. Morin, N. B. Jemaa, D. Jeannot, J. Pinard, and L. Nedelec, "Contacts materials performances under break arc in automotive applications," *IEEE Trans. Compon. Packag. Technol.*, vol. 23, no. 2, pp. 367–375, Jun. 2000, doi: 10.1109/6144.846776.

[139] D. McDonnell, J. Gardener, and J. Gondusky, "Comparison of the switching behavior of silver metal oxide contact materials," in *Proc. IEEE Holm Conf. Electr. Contacts*, Sep. 1993, pp. 37–43, doi: 10.1109/HOLM.1993.489658.

[140] C.-H. Leung, "Arcing contact materials, silver refractory metals," in *Encyclopedia of Tribology*. New York, NY, USA: Springer, 2013, pp. 104–107, doi: 10.1007/978-0-387-92897-5_401.

[141] H. Sone, H. Sugimoto, and T. Takagi, "A measurement on contact resistance and surface profile of arcing Ag contacts," in *Proc. IEEE Holm Conf. Electr. Contracts*, Oct. 1994, pp. 105–109, doi: 10.1109/HOLM.1994.636826.

[142] Z. Wang, W. Li, K. Chen, Z. Li, and S. Shang, "Storage failure mechanism analysis and reliability improvement measures for electromagnetic relay," *IOP Conf. Ser., Mater. Sci. Eng.*, vol. 1043, no. 4, Jan. 2021, Art. no. 042058, doi: 10.1088/1757-899x/1043/4/042058.

LUCAS KIRSCHBAUM received the Dipl.-Ing. degree in deep drilling and petroleum engineering from Technical University Bergakademie Freiberg, Germany, in 2016. He is currently a Ph.D. Researcher with the Centre for Doctoral Training in Embedded Intelligence, Heriot-Watt University, Edinburgh. He is conducting research within the field of PHM of critical assets. His project targets the key elements of this fields of research with a focus on big data analytics. In particular, various approaches are used and applied to the critical assets of the drill string which is particularly exposed to a harsh environment making the implementation of PHM a decisive factor for future operations.

VALENTIN ROBU received the Master of Science degree from Vrije Universiteit, Amsterdam, in 2003, with a specialization in artificial intelligence, and the Ph.D. degree from the TU Eindhoven and CWI, Amsterdam, in 2009. Before October 2020, he was an Associate Professor at Heriot-Watt University, Edinburgh, U.K., where he still holds a visiting appointment. He is currently a Scientific Staff Member at CWI, National Research Institute for Mathematics and Computer Science, Amsterdam, and a part-time Associate Professor, TU Delft, The Netherlands. He is also a Research Affiliate at the Center for Collective Intelligence, Massachusetts Institute of Technology (MIT), USA. He has published over 150 papers in top-ranked journals, conferences and edited volumes, in both the areas of artificial intelligence and electrical engineering. He is a principal investigator or a co-investigator in several energy and AI-focused research projects.

JONATHAN SWINGLER is currently an Associate Professor with the School of Engineering and Physical Sciences (EPS) and an Associate Dean of Heriot-Watt University. Over the last 12 years, he has developed an extensive expertise in the reliability of electrical systems following positions at Loughborough University and the University of Southampton. His work has particularly focused on electrical contacts and inter-connecting in automotive and aerospace systems. He has more than 60 publications, is a reviewer for many leading journal publications, acts as an expert witness concerning failure of components and patent disputes and he is a proposal evaluator and a project reviewer for the European Commission. He is a Chartered Physicist and a fellow of the Institute of Physics.

DAVID FLYNN (Member, IEEE) received the B.Eng. degree (Hons.) in electrical and electronic engineering, the M.Sc. degree (Hons.) in microsystems, and the Ph.D. degree in microscale magnetic components from Heriot-Watt University, Edinburgh, in 2002, 2003, and 2007, respectively. He is currently a Professor of systems engineering with the University of Glasgow. He is also the Founder of the Smart Systems Group (SSG) and an Associate Director of the UKs National Centre for Energy Systems Integration. He has expertise in systems engineering and cyber physical systems (CPS). He is also a Visiting Professor at Heriot-Watt University and also the Vice-Chair of the Institute of Engineering and Technology (IET), U.K. His research explores the challenges, opportunities, and underpinning technologies within cyber physical systems as to promote sustainability and create resilience in systems, organizations, networks, and societies. He teaches smart system integration, electrical engineering, and energy systems.